



Western Michigan University
ScholarWorks at WMU

Master's Theses

Graduate College

4-1995

An Experimental Apparatus for Studying Differential Scattering of Multiply-Charged Ions from Neutral Targets Following Capture

John Edward Edens

Follow this and additional works at: https://scholarworks.wmich.edu/masters_theses

 Part of the Physics Commons

Recommended Citation

Edens, John Edward, "An Experimental Apparatus for Studying Differential Scattering of Multiply-Charged Ions from Neutral Targets Following Capture" (1995). *Master's Theses*. 4272.

https://scholarworks.wmich.edu/masters_theses/4272

This Masters Thesis-Open Access is brought to you for free and open access by the Graduate College at ScholarWorks at WMU. It has been accepted for inclusion in Master's Theses by an authorized administrator of ScholarWorks at WMU. For more information, please contact wmu-scholarworks@wmich.edu.



AN EXPERIMENTAL APPARATUS FOR STUDYING DIFFERENTIAL
SCATTERING OF MULTIPLY-CHARGED IONS FROM
NEUTRAL TARGETS FOLLOWING CAPTURE

by

John Edward Edens

A Thesis
Submitted to the
Faculty of The Graduate College
in partial fulfillment of the
requirements for the
Degree of Master of Arts
Department of Physics

Western Michigan University
Kalamazoo, Michigan
April 1995

ACKNOWLEDGMENTS

First of all I would like to express thanks to my parents and family for their love and support in this and all of my endeavors.

I would like to express my gratitude to my thesis advisor, Dr. E.Y. Kamber for his invaluable guidance and instruction provided throughout this project. I wish to thank Dr. J.A. Tanis and Dr. S.M. Ferguson for their comments and suggestions as members of my thesis committee.

Next, I would like to acknowledge Jim Cornell and Bob Hiltbrand for their help in the design and construction of the detector assembly and other necessary apparatus. My thanks are also expressed to Kadir Akgüngör, Oliver Voitke and Meenatchi Gopinathan for their friendship and help in keeping me sane.

Lastly, I would like to thank God, without whom none of this could have been possible.

John Edward Edens

AN EXPERIMENTAL APPARATUS FOR STUDYING DIFFERENTIAL
SCATTERING OF MULTIPLY-CHARGED IONS FROM
NEUTRAL TARGETS FOLLOWING CAPTURE

John Edward Edens, M.A.

Western Michigan University, 1995

An experimental apparatus has been designed, enabling measurement of angular differential cross sections for single-electron capture (SEC). The design consists of a microchannel plate detector with a one-dimensional position sensitive anode. A bow-tie shaped aperture was employed to convert a radially scattered distribution into an approximate linear one. An electrostatic retarding grid was used to separate SEC contributions from the reaction products. Measurements were made of the angular differential cross sections for SEC of Ar^{q+} ($q=4-6,8$) ions scattering from He and Ar at impact energies of 600 to 3000 eV and angles between 0 and 23 mrad. The experimental angular spectra contain a main peak lying near a critical angle, θ_c , corresponding to capture at an impact parameter equal to the crossing radius of the active channel. The results for Ar^{6+} and Ar^{8+} on He and Ar are in qualitative agreement with calculations made using a semiclassical model based upon classical differential cross sections coupled with Landau-Zener transition probabilities.

TABLE OF CONTENTS

ACKNOWLEDGMENTS.....	ii
LIST OF TABLES.....	vi
LIST OF FIGURES.....	vii
CHAPTER	
I. INTRODUCTION.....	1
II. THEORETICAL CONSIDERATIONS.....	5
Kinematics.....	6
Semiclassical Curve-Crossing Model.....	9
Introduction.....	9
Adiabatic and Diabatic Potentials.....	9
Adiabatic and Diabatic Behavior.....	10
Coulombic Potential Curves.....	12
Crossing Radii.....	13
Classical Differential Cross Section.....	14
Landau-Zener Transition Probabilities....	20
Multichannel Landau-Zener Model.....	23
Features of Angular Distribution Spectra....	24
Half Coulomb Scattering Angle.....	24
Rainbow Angle.....	25
Stueckelberg Oscillations.....	26
III. EXPERIMENTAL APPARATUS.....	28
Production of the Pump Beam.....	28

Table of Contents--Continued

CHAPTER

Recoil Ion-Beam Production.....	31
Collision Gas Cell.....	34
Detector Assembly.....	35
Bow-Tie Collimator.....	35
Retarding Grid Potential Analyzer.....	36
Microchannel Plates.....	38
Resistive Anode Encoder.....	39
Data Acquisition.....	40
IV. DATA ANALYSIS.....	45
Charge State Spectroscopy.....	45
Energy Analysis.....	47
Angular Distribution.....	48
Angular Resolution.....	50
Background Subtraction.....	51
Data Smoothing.....	53
Theoretical Calculations.....	53
V. RESULTS AND DISCUSSION.....	59
Two-State Model.....	60
Ar ^{q+} - He (q=4-6) Collision Systems.....	60
Ar ^{q+} - Ar (q=4-6) Collision Systems.....	63
Semiclassical Multichannel Model.....	65

Table of Contents--Continued

CHAPTER

Ar ^{q+} - He (q=6,8) Collision Systems.....	65
Ar ^{q+} - Ar (q=6,8) Collision Systems.....	67
VI. CONCLUSION.....	71
BIBLIOGRAPHY.....	74

LIST OF TABLES

1.	Electron Transition Energy Levels Used for $\text{Ar}^{4+} (3p^2 \ ^3P)$ - He Collisions.....	55
2.	Electron Transition Energy Levels Used for $\text{Ar}^{5+} (3s^2 \ 3p \ ^2P)$ - He Collisions.....	55
3.	Electron Transition Energy Levels Used for $\text{Ar}^{6+} (3s^2 \ ^1S)$ - He Collisions.....	56
4.	Electron Transition Energy Levels Used for $\text{Ar}^{8+} (2p^6 \ ^1S)$ - He Collisions.....	56
5.	Electron Transition Energy Levels Used for $\text{Ar}^{4+} (3p^2 \ ^3P)$ - Ar Collisions.....	57
6.	Electron Transition Energy Levels Used for $\text{Ar}^{5+} (3s^2 \ 3p \ ^2P)$ - Ar Collisions.....	57
7.	Electron Transition Energy Levels Used for $\text{Ar}^{6+} (3s^2 \ ^1S)$ - Ar Collisions.....	58
8.	Electron Transition Energy Levels Used for $\text{Ar}^{8+} (2p^6 \ ^1S)$ - Ar Collisions.....	58
9.	Compilation of Data and Results Using Two-State Model.....	60

LIST OF FIGURES

1.	Classical Representation of a Collision Involving Single-Electron Capture.....	7
2.	Schematic Drawing of Diabatic and Adiabatic Potential Curves.....	11
3.	Two-State Diabatic Potential as a Function of Internuclear Distance.....	16
4.	Two-State Picture of Trajectories for Capture on the Way in (Above) and Capture on the Way out (Below).....	18
5.	Typical Deflection Function for Two-State Collision Process.....	26
6.	Schematic Diagram of the Western Michigan University Tandem Van de Graaff Accelerator Laboratory.....	29
7.	Schematic of the Experimental Apparatus and Detector System Used to Measure the Differential Cross Sections for Single-Electron Capture.....	32
8.	Retarding Grid Voltage Scan for Product Projectile Ions for the Collision $\text{Ar}^{5+}\text{-He}$	37
9.	Electronics Block Diagram for Angular Distribution Measurements.....	41
10.	Electronics Block Diagram for Recoil-Ion Charge State Analysis and Retarding Grid Voltage Scans of Reaction Products.....	43
11.	Typical Charge-State Spectrum for Argon Recoil Ions Produced in the Recoil-Ion Source.....	45
12.	Square Root of Mass-to-Charge Ratio of Argon Recoil Ions Plotted as a Function of the Analyzing Magnet Current.....	46

List of Figures--Continued

13. Charge Separation of Product Projectile Ions for the Collision $\text{Ar}^{6+}\text{-He}$	48
14. Schematic of the Experiment Showing How Measured Distances Across the Detector Were Converted to an Angular Distribution.....	49
15. Position Calibration Spectrum Used in the Conversion From Channel Numbers to Scattering Angle.....	50
16. Typical Angular Resolution of an Ar^{4+} Ion Beam.....	51
17. Typical Background Subtraction Process for Angular Distribution Spectra. The Arrows Indicate the Center of the Bow-Tie Collimator.....	52
18. Angular Differential Cross Sections for Ar^{q+} on He for $q = 4\text{-}6$. Arrows Indicate Position of θ_c . Data Appear as Points; Smooth Curves are Fits to the Data.....	62
19. Angular Differential Cross Sections for Ar^{q+} on Ar for $q = 4\text{-}6$. Arrows Indicate Position of θ_c . Data Appear as Points; Smooth Curves are Fits to the Data.....	64
20. Angular Differential Cross Sections for $\text{Ar}^{6,8+}$ on He. Data Appear as Points, Smooth Curves as Fits and Theoretical Calculations as o's.....	66
21. Angular Differential Cross Sections for $\text{Ar}^{6,8+}$ on Ar. Data Appear as Points, Smooth Curves as Fits and Theoretical Calculations as o's.....	69

CHAPTER I

INTRODUCTION

Among the principal topics for research in atomic physics is the study of collisions involving atomic and molecular particles. Three fundamental processes may occur as a result of ion-atom collisions: excitation, ionization or charge transfer, i.e. electron capture. Combinations of the above three may also result. Of particular interest is single-electron capture from rare gas atoms by multiply-charged ions, since this is a predominant reaction at low energies.

The importance of electron capture research is understood by the variety of physical phenomena which involve this process. Charge transfer processes involving multiply-charged ions are of interest in the study of astrophysical plasmas where they have been found to modify the ionization structure of plasmas and exert a major influence on plasmas created by the absorption of high frequency radiation. Also, charge transfer into excited states may radiate, resulting in emission lines which can be used as a diagnostic probe of the physical environment and nature of the ionizing source (Dalgarno, 1985). Another use of charge transfer was proposed by Louisell et

al., (1974) for the investigation of a soft x-ray laser, in which inversion is produced by deexcitation of an electron captured into a metastable state of a bare helium nucleus from a hydrogen atom (Louisell et al., 1974). Also of significant interest is the development of an understanding of interactions of many-body systems; that is, between the nuclei and electrons of both the projectile ion and target atom (Waggoner, 1990).

Much of the earlier research involving ion-atom collisions resulting in charge transfer were concerned with total cross section and final-state selective measurements. Many of these measurements utilized translational energy spectroscopy; that is, measurement of the kinetic energy gained or lost by the projectile as a result of the collision reaction. Electron and photon spectroscopy are also methods which have been used to make state-selective measurements. There also exist, although to a lesser extent, measurements of the angular distributions in charge-transfer events.

Previous measurements of the angular distributions for single-electron capture have been reported by several authors. Cocke et al., (1987a) studied angular distributions for systems of Ne^{q+} and Ar^{q+} ($q=3-8$) on targets of He, D_2 , and Ar at accelerating voltages between 40 and 350 V. In particular, for Ar^{8+} -Ar, they resolved contributions due

to single-electron capture and transfer ionization. Tunnel et al. (1987) have measured angular distributions of product Ne ions for Ne^{q+} ($q=3-6$) capturing electrons from He at laboratory energies between 172 and 1200 eV. They report for $q=4$ that distributions are strongly peaked in the forward direction, while for $q=3,5$ and 6, the reaction products are concentrated at larger scattering angles. Waggoner (1990) measured angular distributions for single-electron capture from He by Ar^{6+} ions at laboratory impact energies between 296 and 1287 eV. Their distributions were qualitatively explained by a simple two-state diabatic curve-crossing model. Cocke et al. (1987b) have measured angular distributions for a variety of projectiles capturing single electrons from targets of He, Ar. and D_2 . They report that the population of the s-state with nonbare projectiles results in forward peaking. More recently, Andersson et al. (1991) report angular differential cross sections for one-electron capture in Ar^{6+} -He collisions at very low energies (1.6-13eV/u). For this system, they find an unexpectedly high probability for single-electron capture with projectile core excitation, a process referred to as transfer excitation (TE).

The purpose of this present work is two fold. First, to develop a detector assembly for the measurement of the angular distributions for single-electron capture.

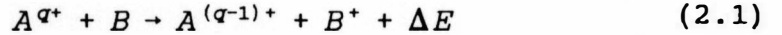
Secondly, to investigate the angular distributions for single-electron capture by Ar^{q+} projectile ions ($q=4-6,8$) from He and Ar at impact energies between 600 and 3000 eV, the results of which will be compared with a theoretical model developed from a semi-classical approach.

Chapter II will include theoretical aspects that have been considered. Chapter III consists of a description of the experimental apparatus used for the measurements. Techniques for data analysis will be given in Chapter IV. In Chapter V, experimental results and a discussion of individual collision systems as compared with expectations will be treated. Lastly, conclusions drawn from the above results and prospects for future work will be discussed.

CHAPTER II

THEORETICAL CONSIDERATIONS

Single-electron capture has been found to be the most probable event as the result of low-energy ion-atom collisions (Kamber and Cocke, 1991). This process of charge transfer, by which an electron from a neutral target, B, is captured to a multiply-charged ion, A, can be represented by the expression,



where q is the initial charge state of the projectile ion and ΔE is the energy defect of the reaction channel involved.

Besides single-electron capture, capture of multiple electrons, i.e., double-electron capture, and transfer ionization have also been known to contribute significantly for some collision systems (Waggoner, 1990). Transfer ionization is the process whereby double-electron capture occurs to doubly excited states of the projectile and, subsequently, one electron is lost by the projectile due to autoionization.

The focus of this chapter involves the theoretical aspects of the model used for determining the electron-

capture angular distributions for the collision systems studied experimentally. Hence, the main ideas of the theoretical methods will be investigated as applied to the model used, without great emphasis upon the formal calculations or the approximations made.

Kinematics

A kinematic picture of the collision process involving single-electron capture is shown in Figure 1. The collision between the projectile ion and target atom is an inelastic one and is characterized by a change in internal energy. The energy defect, as introduced in equation 2.1, is defined as the total change in internal energy for the collision. The reaction may be characterized as exoergic or endoergic. For an exoergic reaction, distinguished by a positive energy defect, an increase in kinetic energy is experienced with a corresponding decrease in internal energy. An endoergic reaction consists of an increase in internal energy with a corresponding decrease in kinetic energy; the energy defect being negative. The energy defect may be expressed as (Kamber and Cocke, 1991),

$$\Delta E = I(A^{q+}) - I(B) - E_j \quad (2.2)$$

where $I(A^{q+})$ and $I(B)$ are the ionization potentials of the projectile ion and target atom with the captured electron

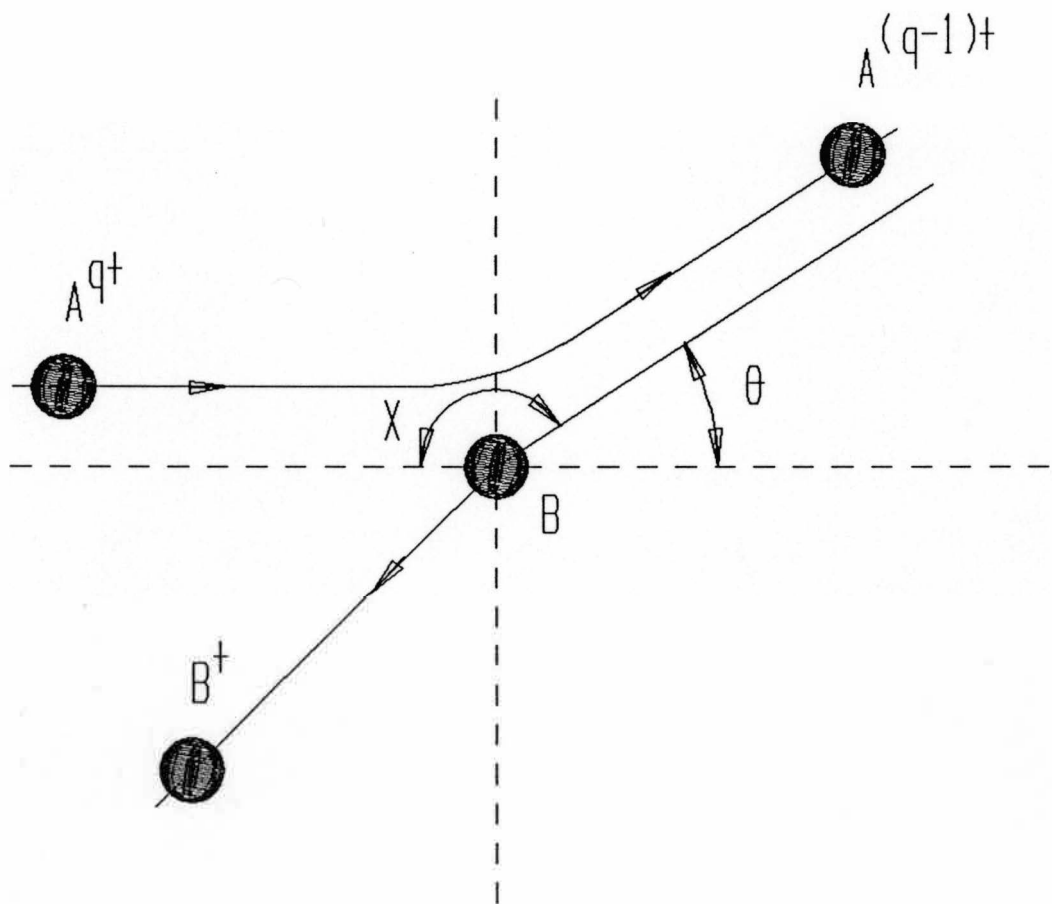


Figure 1. Classical Representation of a Collision Involving Single-Electron Capture.

being assumed as the most loosely bound and the target atom in its ground state. E_j is the excitation energy of the j th level of the projectile ion. It is presently known that the electron is captured into states of the projectile which favor an exoergic reaction (Tunnell, 1986). The kinetic energy gained is shared by both the projectile and target product ions. The distribution of the shared kinetic energy to each reactant depends upon the initial velocity of the projectile ion, the angle into which the projectile is scattered, and the relative masses of the collision partners. Commonly, one defines the quantity which represents the energy gained by the projectile ion as a result of the collision as the Q -value of the reaction. This value is significant since it can be determined experimentally, as when translational energy spectroscopy is employed. The Q -value is defined as (Kamber and Cocke, 1991),

$$Q = E_f - E_i = \Delta E - \Delta K \quad (2.3)$$

where E_f and E_i are the initial and final kinetic energies of the projectile ion, ΔE is the energy defect, and ΔK is the translational energy given to the target.

Semiclassical Curve-Crossing Model

Introduction

In this section, the theoretical aspects behind the semiclassical curve-crossing model used to describe single electron capture will be discussed. The model is called semi-classical because the trajectories of the collision reactants are explained by classical mechanics, while the electron's behavior is described by quantum mechanics. The Born-Oppenheimer approximation, which for slow collisions where the velocities of the nuclei are much lower than those of the electrons, allows for treating, separately, the motion of the electrons and that of the nuclei. Thus, deflection functions and differential cross sections are determined classically, while probabilities for charge transfer are determined using the Landau-Zener formula. For a particular reaction, we calculate a differential cross section for each path leading to a particular state, multiply each by its corresponding transition probability, and then sum them to determine the total differential cross section.

Adiabatic and Diabatic Potentials

During a collision, slow reactants are described as forming a quasimolecule whereby atomic energy levels are

connected by way of molecular ones. Charge transfer occurs as a result of transitions between these molecular electronic states. Potential curves describing the behavior of the ion-atom system during the collision may be determined by solving the Schroedinger equation for the molecular electronic states and adding the repulsive nuclear energy to that of the electronic binding energy. The potential curves obtained are adiabatic in the sense that they are prohibited from crossing one another. This is a consequence of the Neumann-Wigner non-crossing rule that does not allow molecular energy levels of the same symmetry to cross (Waggoner, 1990). However, another set of potential curves are allowed to pass smoothly through each other. These diabatic curves violate the non-crossing rule, but are often used to describe charge transfer reactions. Figure 2 shows a set of adiabatic and diabatic potentials. The model utilized in this study makes use of diabatic potentials and thus, unless noted otherwise, the discussions that follow will pertain only to these.

Adiabatic and Diabatic Behavior

Regardless of the type of potentials used, it is the behavior of the system, at or near the curve-crossing or avoided curve-crossing that is significant. Thus, we describe the behavior of the system, at this point, as

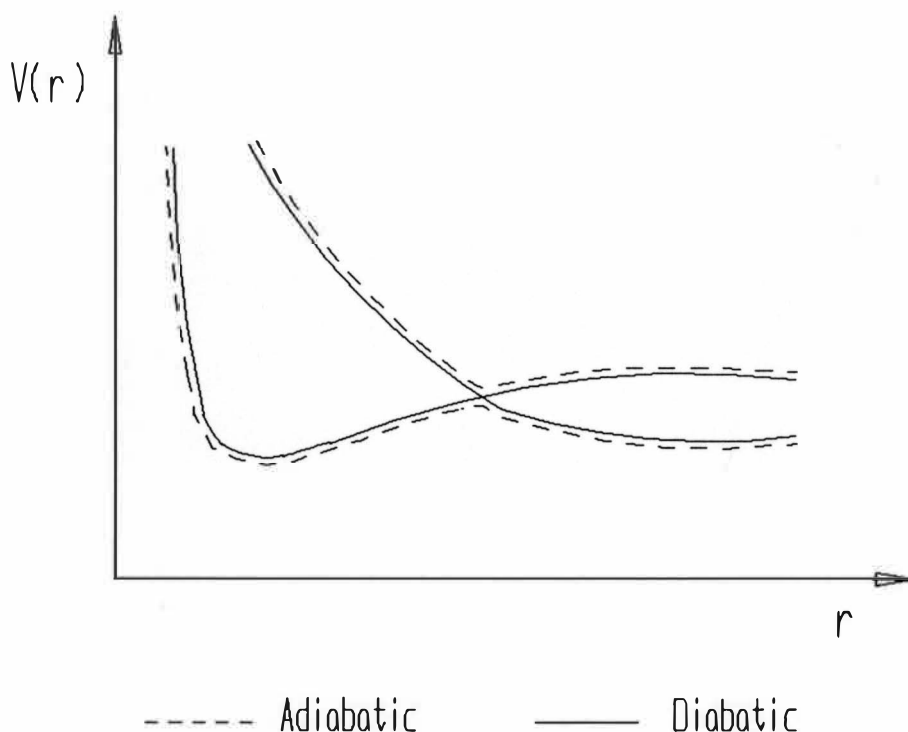


Figure 2. Schematic Drawing of Diabatic and Adiabatic Potential Curves.

being either diabatic or adiabatic. Diabatic behavior corresponds to electron transfer for adiabatic potentials and thus pertains to the jumping from one potential to another at the avoided crossing. For diabatic potentials, this behavior results in no transfer and occurs when the system remains on the same potential while traversing a crossing. Concerning adiabatic behavior, the system would remain on the same potential at an avoided crossing for adiabatic potentials (no transfer); while it would change potentials at a crossing for diabatic potentials (transfer).

Coulombic Potential Curves

Having briefly discussed how potential curves are obtained, no mention has been made of the difficulties in interpreting them. Diabatic potentials are ambiguous to interpret, especially near a crossing where there exists little or no explanation of how they cross. Furthermore, the deflection functions must be calculated numerically since expressions for the curves cannot be obtained analytically. These aforementioned dilemmas are rendered negligible, however, because, in the theoretical model used, zero potential is assumed for the entrance channel and a Coulombic potential is assumed for the exit channel. Charge transfer for slow collisions usually occurs at large internuclear separations. At such distances, the nuclear interaction between the collision reactants should be screened by inner electron clouds hence giving zero initial interaction,

$$V_i(R) = 0. \quad (2.4)$$

After capture, the product projectile exits with charge $+(q-1)$ and the target with charge $+1$. Thus, a repulsive Coulombic force results. Accounting for the system's overall loss of internal energy, ΔE (the energy defect), the final potential may be expressed as (Waggoner, 1990)

$$V_f(r) = \frac{(q-1)}{r} - \Delta E, \quad (2.5)$$

where r is the internuclear distance and q is the initial charge state of the projectile ion. This final potential (exit channel) represents the state into which the electron is captured. It is the value of the energy defect which characterizes the particular state to which capture occurs. For the model, relevant energy defects are chosen by referring to the experimental results of the translational energy spectra for the collision systems at similar energies.

Crossing Radii

For reasons previously mentioned and for others that shall be discussed soon, the behavior of the systems near or at the curve crossing is important. These crossing radii, R_x , can be calculated in terms of the energy defect from the condition (Waggoner, 1990),

$$V_i(R_x) = V_f(R_x). \quad (2.6)$$

The resulting expression for the crossing radii is

$$R_x = \frac{(q-1)}{\Delta E}. \quad (2.7)$$

At smaller internuclear distances, inside the crossing radius, there commonly exists capture channels more

exoergic than the active channel which behave adiabatically at crossings with the incident channel. Therefore, the incident channel will not remain flat inside the active crossing, but rather will be promoted to a repulsive potential curve. The proximity of this promotion channel with respect to the active crossing is important in determining the angular distribution of reaction products as will be seen later. With an equation analogous to that of 2.7, and a different value for the energy defect, the crossing radius for this promotion channel may be found. The energy defect is commonly chosen as that for transfer to the nearest low lying level to that of the active capture channel.

Classical Differential Cross Section

Thus far, discussion has focussed on potential curves which are used to describe the interaction between ion-atom pairs resulting in charge transfer collisions. The next step is to make use of these potentials to calculate the angular distribution spectra, i.e., the differential cross sections, $d\sigma/d\theta$. For the calculations and formulae that follow, use will be made of the center-of-mass coordinate system with the recognition that transformation to lab coordinates is imperative before comparison with experimental results. An expression for the classical differential

cross section is given by (Waggoner, 1990),

$$\frac{d\sigma}{d\theta} = \Sigma 2\pi b_i \left| \frac{db}{d\theta} \right|_i. \quad (2.8)$$

To solve for the above, we obviously need an expression relating b , the impact parameter, and θ , the scattering angle. Such an expression, the deflection function, can be obtained by solving the orbit equation which gives the integrated angle, χ , between the incoming and outgoing asymptotes, as seen in Figure 1 (Andersson, 1986)

$$\chi = \int_{ORB} \frac{b|dr|}{r^2 \sqrt{\left(1 - \left(\frac{V(r)}{E_o}\right) - \left(\frac{b}{r}\right)^2\right)}}, \quad (2.9)$$

where r is the internuclear distance, $V(r)$ is the potential, and E_o is the initial projectile center-of-mass kinetic energy. The scattering angle is the angle between incoming and outgoing directions and is related to χ by $\theta = \pi - \chi$. For repulsive scattering, the scattering angle becomes (Andersson, 1986),

$$\theta = \pi - \int_{ORB} \frac{b|dr|}{r^2 \sqrt{\left(1 - \left(\frac{V(r)}{E_o}\right) - \left(\frac{b}{r}\right)^2\right)}}. \quad (2.10)$$

The integral must be broken into several parts to account for the change in potential along the trajectory of the projectile. For a two-state channel, i.e., one entrance

and one exit channel, there are two possible paths the system may follow for charge transfer. The limits of integration for the integral will depend upon the trajectory followed. In Figure 3, a crossing of two diabatic curves is displayed. In the incident channel, the states of the projectile ion, A^{q+} , and target atom, B, are α and β , respectively. For the final channel, one electron has been transferred from the target to the projectile. The final states of the projectile and target are α' and β' . The trajectory will follow one of two paths depending upon how capture takes place, on the "way in" or on the "way out".

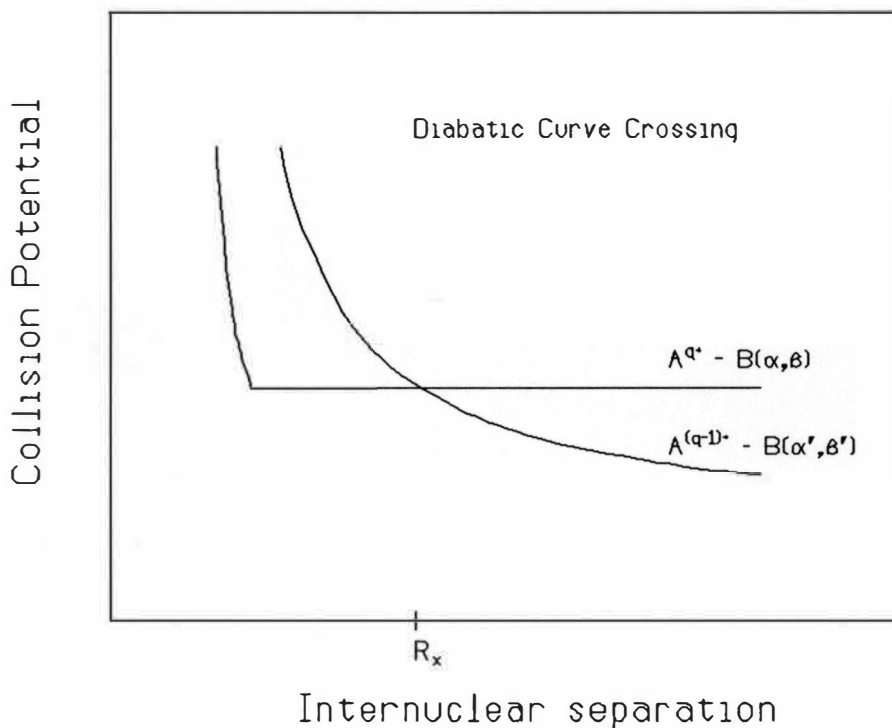


Figure 3. Two-State Diabatic Potential as a Function of Internuclear Distance.

For capture to occur on the way in, an adiabatic transition must occur at the initial encounter of the crossing radius, R_x . The system then proceeds on the Coulombic curve until reaching a turning point, R_t . Next, the system behaves diabatically at the second juncture of the crossing radius, remaining on the Coulomb curve. Figure 4 shows the trajectory for capture on the way in. The limits of integration for the deflection function integral, for this particular trajectory, are expressed as (Waggoner, 1990),

$$\theta = \pi - \int_{R_x}^{\infty} \frac{b dr}{r^2 \sqrt{1 - (\frac{b}{r})^2}} - \int_{R_t}^{R_x} \frac{b dr}{r^2 \sqrt{1 - \frac{V_x(r)}{E_o} - (\frac{b}{r})^2}} - \int_{R_t}^{\infty} \frac{b dr}{r^2 \sqrt{1 - \frac{V_x(r)}{E_o} - (\frac{b}{r})^2}} \quad (2.11)$$

For capture on the way out, the system behaves diabatically at the first encounter of the crossing radius and thus passes through R_x , traversing the entrance channel onto the promotion channel until a turning point, R_t , is reached. Charge transfer eventually occurs on the way out at the second passing of the crossing radius, R_x , where the system behaves adiabatically. Figure 4 displays the resulting trajectory for charge transfer on the way out. The expression representing the integral for the deflection function is (Waggoner, 1990)

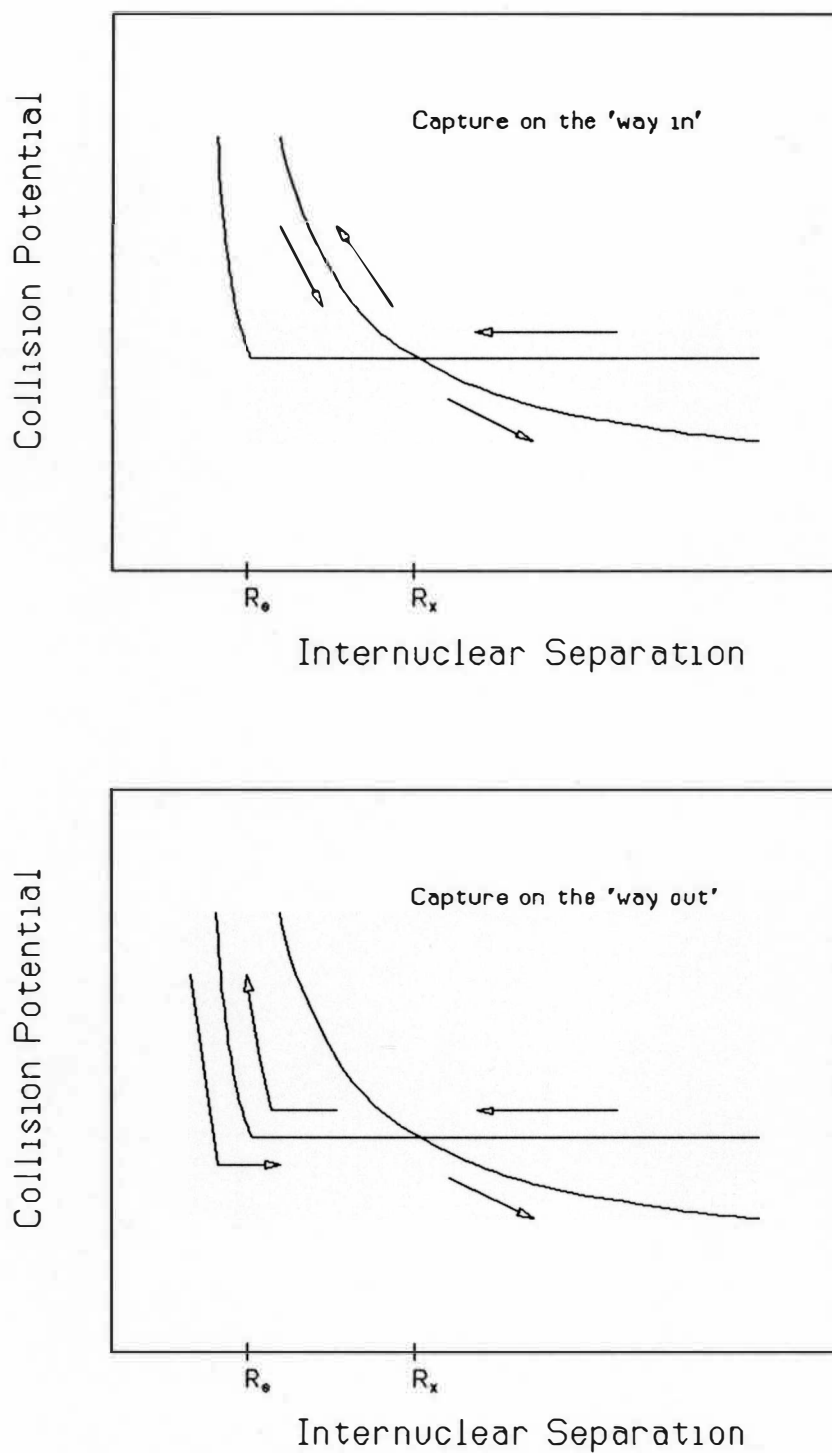


Figure 4. Two-state Picture of Trajectories for Capture on the Way in (Above) and Capture on the Way out (Below).

$$\theta = \pi - \int_{R_x}^{\infty} \frac{b dr}{r^2 \sqrt{1 - (\frac{b}{r})^2}} - 2 \int_{R_s}^{R_x} \frac{b dr}{r^2 \sqrt{1 - (\frac{b}{r})^2}} - 2 \int_{R_t}^{R_s} \frac{b dr}{r^2 \sqrt{1 - \frac{V_s}{E_o} - (\frac{b}{r})^2}} - \int_{R_x}^{\infty} \frac{b dr}{r^2 \sqrt{1 - \frac{V_f}{E_o} - (\frac{b}{r})^2}}, \quad (2.12)$$

where R_s is the internuclear separation at which the initial channel meets the promotion channel.

Having expressed the differential cross section using center-of-mass coordinates, it becomes necessary to express the differential cross section in laboratory coordinates in order to compare with experimental results. Using classical mechanics, eventually we determine an expression for the differential cross section in the lab frame (Waggoner, 1990),

$$\left(\frac{d\sigma}{d\theta} \right)_{lab} = \left(\frac{d\sigma}{d\theta} \right)_{CM} \frac{\gamma^2 + 2\gamma \cos\theta + 1}{\gamma \cos\theta + 1}, \quad (2.13)$$

where,

$$\gamma = \frac{m_1}{m_2} \left(1 + \frac{\Delta E_x}{E_o} \right)^{-\frac{1}{2}}, \quad (2.14)$$

with ΔE being the energy defect, E_o the initial projectile kinetic energy, and m_1 , m_2 the masses of the projectile and target, respectively. Therefore, it is necessary to differentiate the expressions for the scattering angles obtained from the integrals for the classical deflection

functions (equations 2.11 and 2.12) in order to obtain the classical differential cross sections in the lab system.

This two-channel case, previously spoken of, can be generalized to one in which there are multiple paths which lead to the same final states of the collision system. Each path will have a unique trajectory and a differential cross section contributing to the total differential cross section. Each trajectory will also have a corresponding probability. Thus, by multiplying each contribution of the classical differential cross section with its corresponding probability, and summing these, the model employed leads to a value for the total semiclassical differential cross section for electron capture to a particular final state on the product projectile ion. Hence, the next topic of interest is the probability for charge transfer. To simplify the discussion, the two-channel situation will be explained, later generalizing to the multiple-channel case.

Landau-Zener Transition Probabilities

Generally, p is defined to be the probability that upon encountering a curve crossing, the system behaves diabatically and remains on the same potential curve. Then $(1-p)$ is the probability that an adiabatic transition occurs and the system changes potential curves at the crossing radius. Thus, each of the two possible paths, $p^{(i)}$,

has a probability (Andersson, 1986),

$$p^{(1)} = p^{(2)} = p(1-p). \quad (2.15)$$

The total probability for transition is then,

$$p_T = p^{(1)} + p^{(2)} = 2p(1-p). \quad (2.16)$$

The single-crossing transition probability, that is, the probability that the system remains on a diabatic potential curve when traversing a crossing radius, is given by the Landau-Zener model. This probability is (Andersson, 1986)

$$p(b) = e^{-2\pi\gamma}, \quad (2.17)$$

with

$$\gamma = \frac{H_{12}^2}{v_r |\Delta F|}. \quad (2.18)$$

Here, v_r is the radial velocity at the crossing radius, R_x , and is given by

$$v_r = v_o \left[1 - \left(\frac{b}{R_x} \right)^2 \right]^{\frac{1}{2}}, \quad (2.19)$$

where v_o is the initial velocity and b is the impact parameter. The quantity ΔF is given by

$$\Delta F = \left(\frac{d}{dR} (U_1 - U_2) \right)_{R=R_x}, \quad (2.20)$$

where U_1 and U_2 are the entrance and exit potentials.

Substituting for the potentials used, zero for entrance channel and Coulombic for exit channel, equation 2.20 becomes (Andersson, 1986)

$$\Delta F = \frac{(q-1)}{R_x^2} . \quad (2.21)$$

The coupling element, H_{12} , was determined semi-empirically by Olson and Salop (1976) and is expressed as

$$H_{12}^{os} = 9.13 q^{-\frac{1}{2}} \exp(-1.324 \alpha R_f q^{-\frac{1}{2}}) \quad (2.22)$$

where α is a parameter introduced to allow for target atoms other than hydrogen, specifically

$$\alpha = (2I_t)^{\frac{1}{2}} \quad (2.23)$$

with I_t being the ionization potential of the alternative target atom.

To account for projectile ions which are only partially stripped, a correction term derived by Taulbjerg has been added to the coupling element. This term depends on the quantum numbers n and l of the state into which the electron has been transferred onto the projectile ion and is expressed as (Taulbjerg, 1986),

$$f_{nl} = \frac{(-1)^{n+l-1} (2l+1)^{\frac{1}{2}} \Gamma(n)}{[\Gamma(n+l+1) \Gamma(n-1)]^{\frac{1}{2}}} . \quad (2.24)$$

Thus, the corrected coupling element is given by

$$H_{12} = f_{nl} H_{12}^{os}. \quad (2.25)$$

Multichannel Landau-Zener Model

When generalizing the two-state situation to a multiple-state one, additional Coulombic potentials, each pertaining to a particular state on the projectile, intersect the entrance channel. These result in additional paths that may be traversed for capture into a particular final state. The probability p_n ($n=1,2,\dots,N$) for capture into the n th final state, (assuming that there is no interference between different paths leading to a particular channel), is (Olson and Salop, 1976)

$$p_n = p_1 p_2 \dots p_n (1 - p_n) [1 + (p_{n+1} p_{n+2} \dots p_N)^2 + (p_{n+1} p_{n+2} \dots p_{N-1})^2 (1 - p_N)^2 + (p_{n+1} p_{N-2})^2 + (1 - p_{N-1})^2 + \dots + p_{n+1}^2 (1 - p_{n+2})^2 + (1 - p_{n+1})^2]. \quad (2.26)$$

Then, the expression used for the semiclassical cross section in the theoretical model for single electron capture is obtained (Andersson, 1986),

$$\left(\frac{d\sigma}{d\theta}\right)_{lab} = \sum p_n^j \left(\frac{d\sigma}{d\theta}\right)_{lab}^j, \quad (2.27)$$

where j corresponds to the particular trajectories that were traversed to obtain the final state on the projectile ion.

Features of Angular Distribution Spectra

Recollecting the two-channel potential curve picture, the two possible paths that may be followed by the system result in a double-branched deflection function, as shown in Figure 5. The upper branch of the deflection function relates to the trajectory followed for electron capture on the way in, whereas the lower branch pertains to the trajectory followed for electron capture on the way out. Electron capture on the way in usually results in large angle scattering, while capture on the way out typically extends to small angles, giving rise to an angular distribution which is forward peaked. Features on the deflection function represent physical phenomena of the collision.

Half Coulomb Scattering Angle

The angle θ_c , known as the critical angle or half Coulomb scattering angle, is the scattering angle corresponding to capture at an impact parameter equal to the crossing radius. The position of the critical angle in angular distribution spectra is considered a threshold angle for electron capture. According to the theoretical model used, charge transfer cannot occur until the collision system has reached the crossing radius, R_x . Thus the probability for transition at $b > R_x$ is zero. Since no

Coulomb interaction occurs until the projectile travels within the crossing radius, the collision becomes a half-Rutherford event and the critical angle, in center-of-mass coordinates, can be shown to equal half the Rutherford scattering angle associated with the Coulomb potential of the reaction products after capture (Waggoner, 1990),

$$\theta_c = \frac{1}{2} \theta_R. \quad (2.28)$$

For small scattering angles, the center of mass critical angle becomes (Waggoner, 1990)

$$\theta_c = \frac{1}{2} \theta_R = \frac{\Delta E}{2E_0}, \quad (2.29)$$

where ΔE is the energy defect and E_0 is the initial kinetic energy of the projectile.

Rainbow Angle

Another feature of the deflection function is the discontinuity in the lower branch occurring at scattering angle, θ_r , which corresponds to the smallest angle for which two impact parameters result in the same scattering angle. In Figure 5, this occurs at crossing radius, R_c . The discontinuity is a consequence of a change in functional form, from zero potential to pure Coulombic potential, of the expressions used to calculate the integral in equation

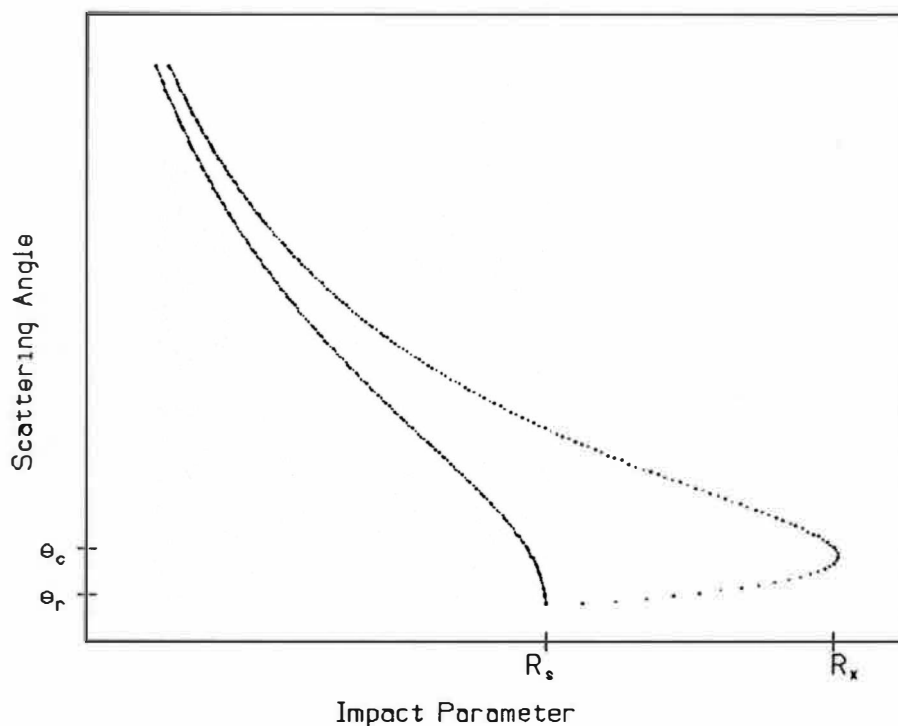


Figure 5. Typical Deflection Function for Two-State Collision Process.

2.12. The result of the discontinuity is the presence of a maximum in the differential cross section, known as a rainbow effect. Classically, this effect occurs when the scattering from a very large number of impact parameters results in the same scattering angle.

Stueckelberg Oscillations

Once again we turn to the deflection function and its two branches, the result of the two possible trajectories that may be followed. The amplitudes from the two trajec-

tories may interfere resulting in oscillations due to constructive and destructive interference which should then appear in the angular distribution. These are known as Stuekelberg oscillations. However, in most cases, these oscillations are too rapid to be observed within experimental resolution.

CHAPTER III

EXPERIMENTAL APPARATUS

As previously stated, this experiment is concerned with the study of single-electron capture as a result of the collision between low-energy multiply-charged ions and rare gas atoms. This chapter is primarily devoted to a discussion of the experimental apparatus which allowed us to make the measurements; the tandem Van de Graaff accelerator, recoil ion source, collision gas cell, position sensitive detector assembly and data acquisition system. Within the paragraphs that follow, a detailed description is presented for each of the significant experimental components that were put to use.

In this work, a fluorine ion beam from the WMU tandem Van de Graaff accelerator was used in the production of recoil ions for use as a secondary projectile ion beam. The primary fluorine ion beam is called a 'pump' beam. A schematic illustrating the WMU accelerator laboratory is shown in Figure 6.

Production of the Pump Beam

The production of the pump beam used in this experiment begins at a negative ion source referred to as 'SNICS'

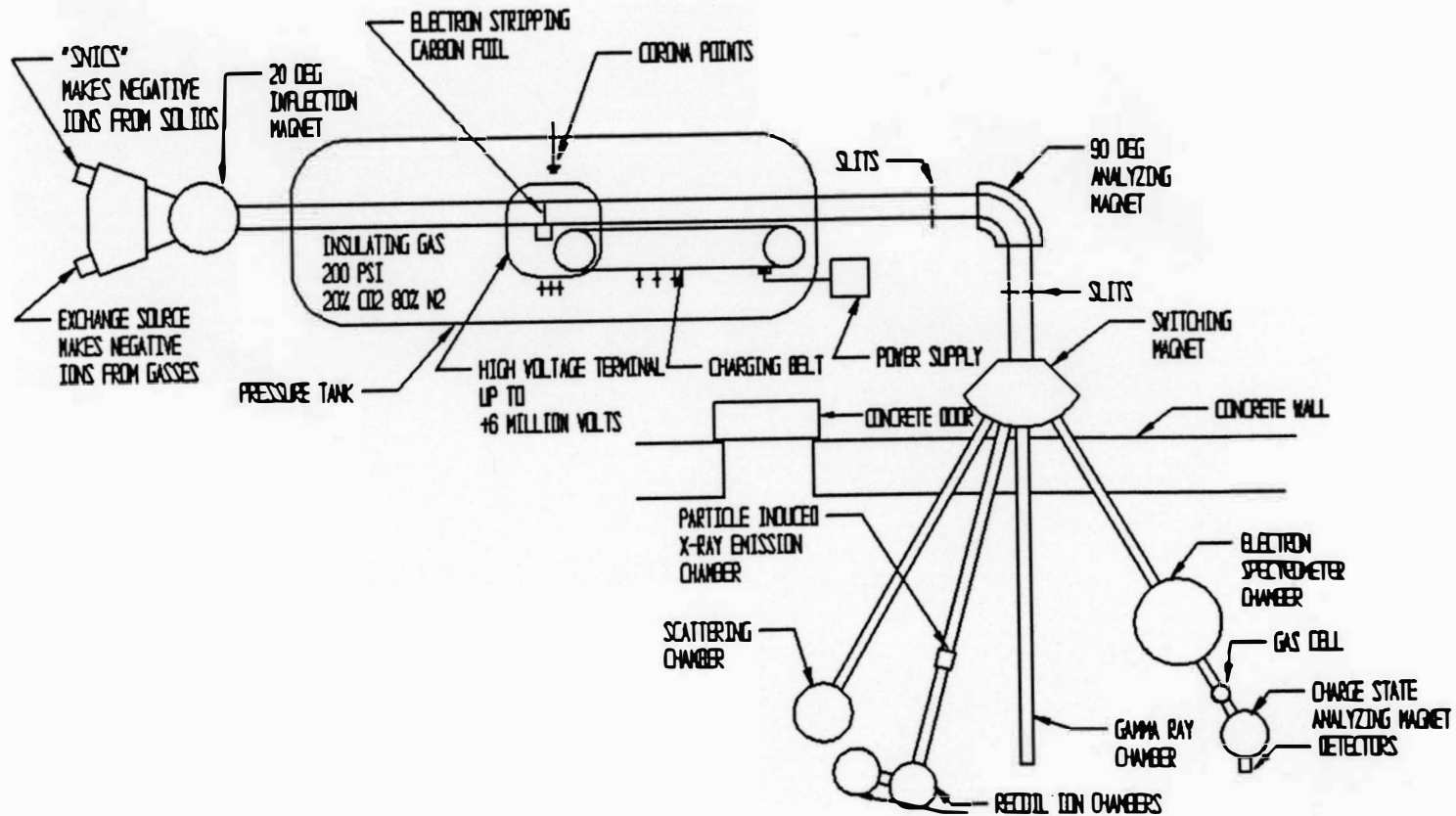


Figure 6. Schematic Diagram of the Western Michigan University Tandem Van de Graaff Accelerator Laboratory.

or source of negative ions by cesium sputtering. Inside of the SNICS, cesium is vaporized in a boiler and allowed to enter the ion source through a valve opening. Within the ion source, there exists a hot tungsten coil set before a sputter cathode which is packed with CaF_2 and held at a negative potential. Cesium atoms become ionized by the coil and the resulting positive ions sputter atoms from the cathode. A number of these sputtered fluorine atoms capture electrons from collisions with cesium and are repelled from the cathode, exiting through an aperture. The whole source, maintained at a negative potential, permits ions to be accelerated towards a grounded extraction electrode and subsequently towards a final focus electrode, that is held at a positive potential. Next, a 20 degree inflection magnet selects the ion species and directs this beam of accelerated ions through an einzel lens which focuses the beam into the low-energy end of the accelerator. Enclosed in the accelerator tank is a high voltage terminal insulated by a high pressure mixture of CO_2 and N_2 . The voltage to the terminal is controlled by corona current flowing to needle points inserted through the side of the tank. The negative ion beam, entering the low energy end, is accelerated towards the terminal, set at approximately 5 MV in this instance. An O_2 gas stripper is located within the terminal, the purpose being to strip the

negative ion beam of electrons, resulting in a beam of positive ions which is repelled from the terminal. The beam exiting the high-energy end of the accelerator impinges on a set of defining slits, hence creating an object for the 90 degree analyzing magnet. The analyzing magnet focuses the ion beam of preferred charge state (and thus preferred energy) onto a set of image slits. Due to energy fluctuations in the beam, there exists some current striking the image slits. This current is fed back to the corona system and used to stabilize the terminal voltage. The ion beam is directed into the desired target room beam line with the aid of a switching magnet.

The pump beam, a 25 MeV F^{4+} beam in our case, enters into a recoil-ion source (RIS), where multiply-charged ions are produced and extracted perpendicular to the pump beam with the application of voltages to potential planes within the source. Hence, a low energy projectile ion beam is formed. An illustration of the experimental apparatus used is shown in Figure 7.

Recoil-Ion Beam Production

Before entrance into the RIS, the pump beam is collimated by four-jaw slits. Upon entering the RIS, the beam interacts with the target gas atoms, generating recoil-ions as it passes through the ion source and is

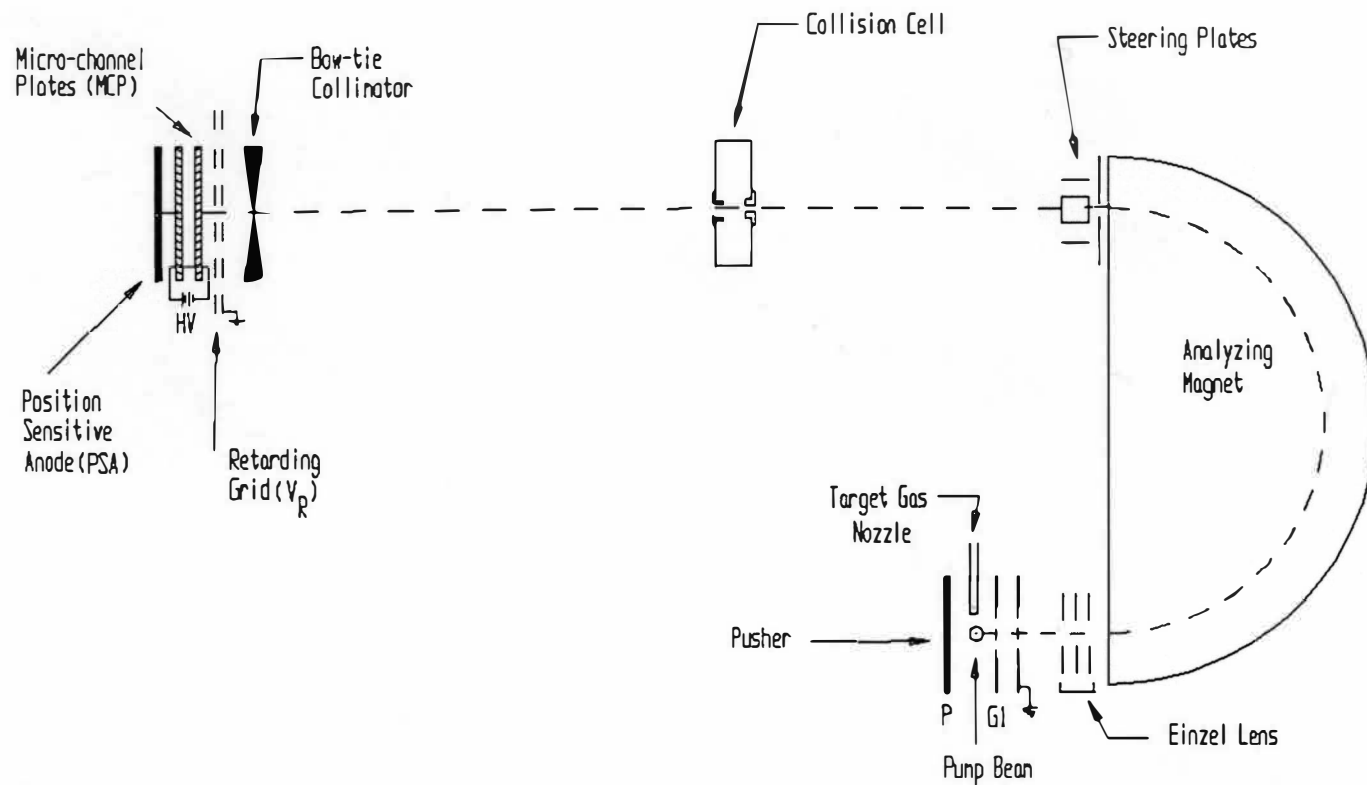


Figure 7. Schematic of the Experimental Apparatus and Detector System Used to Measure the Differential Cross Sections for Single-Electron Capture.

finally collected by a faraday cup. Typical beam currents collected by the faraday cup were between 0.5 and 1 microampere. The RIS is made up of a pusher, nozzle, extracting grid (G1), and a grounded grid. Target gas atoms come into the source through the nozzle; the pressure, held constant, is monitored by noting an increase in the background pressure of the main chamber from about 2×10^{-6} Torr to about 3×10^{-6} Torr. Recoils are extracted via a potential field set up by voltages applied to the pusher, nozzle and extracting grid. Common potentials for the pusher, nozzle and grid were 200, 160, and 140 volts, respectively.

Once extracted, the recoil-ion beam is focused with an einzel lens onto the entrance aperture of a 180 degree double focusing magnet, of radius 13 cm, to be mass analyzed. Charged particles experience a force when traversing a magnetic field that is normal to the direction of both their velocity and the magnetic field. For a beam of charged particles with constant energy per unit charge constrained to move within a given radius, the magnetic field is inversely proportional to the charge to mass ratio of the ions, $B \propto m/q$. Therefore varying the magnetic field of the analyzing magnet permits selection of a specific charge state for our projectile ion beam.

Following mass analysis, the beam is collimated by an

aperture of 12.7 mm and directed with horizontal and vertical parallel deflection plates towards the collision gas cell. It is within this cell that the events of interest take place, namely, single-electron capture from atoms by projectile ions.

Collision Gas Cell

The collision gas cell was constructed of aluminum and is 25.4 mm in length. It was designed so that entrance and exit apertures could be changed. Holes of various diameters were drilled into identical disks that could be bolted to the main body of the cell. For our experiment, 1 mm entrance and 2 mm exit apertures were used. To prevent surface charge build up, which could result in projectile beam deflection, the surface of the cell was covered with dry graphite lubricant. Besides aiding in diminishing surface charge build up, the graphite also reduces secondary emission effects. The cell was attached to a rod which was vacuum sealed through a top flange via two o-rings which allowed for vertical positioning of the cell under vacuum. The whole assembly was mounted on a flange that permitted motion transverse to the beam direction to assist in the alignment of the cell while the system was under vacuum.

The products of the collision reaction next reach the

detector assembly. The assembly was comprised of a bow-tie collimator, retarding grid potential analyzer, and a chevron detector with a one-dimensional resistive anode encoder (see Fig. 7).

Detector Assembly

Bow-tie Collimator

In view of the fact that we employed a detector which was sensitive to only one-dimension, while the products of the collision are radially distributed, a 45-degree bow-tie shaped aperture was used to collimate the products and thus transform a radial distribution into a one-dimensional distribution. This was accomplished by aligning the bow-tie axis with that of the resistive anode encoder, which allows for the position along a single axis to be approximated by $x = \rho \cos \theta \approx \rho$, with maximum and average deviations of x given by 8.2% and 2.7%, respectively (Tunnel, 1986). Beam alignment at the center of the bow-tie was accomplished by the use of micrometers. Four micrometers, set 90 degrees from one another, allowed for vertical and horizontal motion of the detector system while under vacuum.

Following the collision, reaction products contained contributions from single-, double-, and multiple-electron capture events, as well as from that component which did

not undergo charge exchange, i.e., the direct beam. In order to distinguish between components of the scattered products, a retarding grid potential analyzer was used to determine the charge states of the products.

Retarding Grid Potential Analyzer

The voltage applied to a retarding grid potential analyzer establishes an equipotential plane forming a potential barrier to charged particles. For a potential, V , applied to the retarding grid, only particles whose energy surpasses the potential established by the grid, qV (where q is the charge state of the particle), can penetrate the potential barrier. A scan of the retarding grid voltage for $\text{Ar}^{5+}\text{-He}$ at accelerating potential, $V_{\text{acc}} = 197$ V is shown in Figure 8. The vertical axis represents the total number of events detected for a given grid voltage. For grid voltages below V_{db} , all reaction products are collected, i.e., electron capture products along with the direct beam. At grid voltages greater than or equal to V_{db} , the direct beam was suppressed. Thus the accelerated energy of the projectile beam was taken to be that given by retarding grid potential, qV_{db} . The next threshold occurs at V_{sc} ; here products of single-electron capture are suppressed. Hence, at retarding grid voltages above V_{sc} , only events that have experienced double or multiple

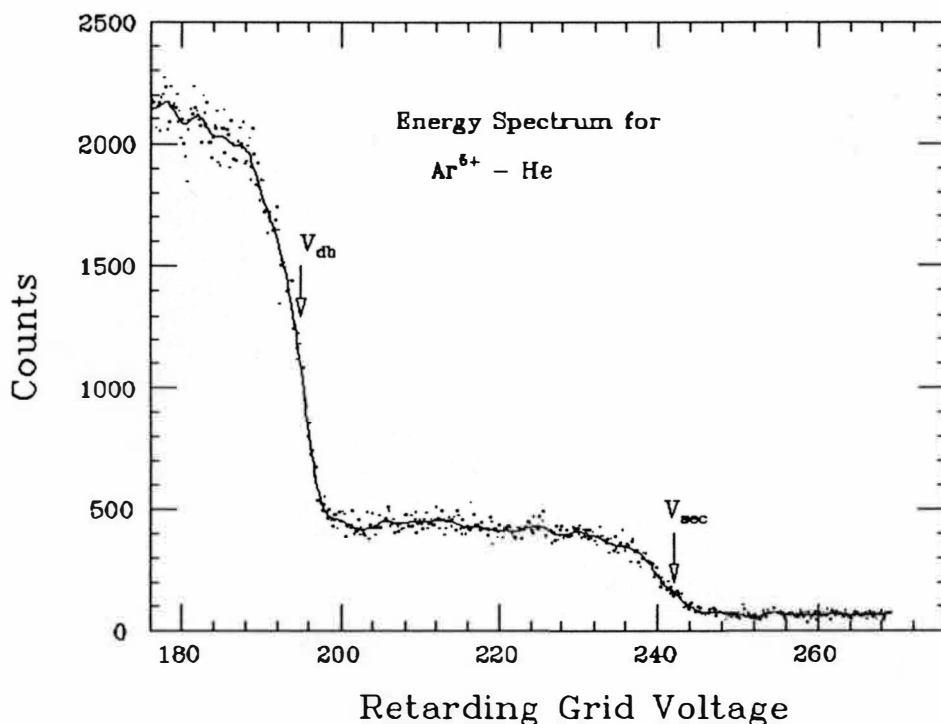


Figure 8. Retarding Grid Voltage Scan for Product Projectile Ions of the Collision $\text{Ar}^{5+} - \text{He}$.

capture events are collected.

Since the focus of this study is on single-electron capture, the potential applied to the grid during data collection, was set between the thresholds for the direct beam, V_{db} , and that for single capture, V_{sec} , with the assumption that the events due to multiple capture could be neglected. However, in some instances, significant contributions came from double and multiple capture events. For such cases, spectra were also taken for these events and subtracted so as to isolate single capture events. For the grid system used, a grounded grid was situated approxi-

mately 4 mm before the retarding grid, while the chevron detector assembly was located at a distance of approximately 1.6 mm behind the retarding grid. Both grids, made of nickel, had 70 lines per inch and 90% transmission.

The reaction products, collimated by the bowtie aperture and filtered by the retarding grid potential analyzer, then impinged upon the chevron detector assembly. This detector system consisted of two microchannel plates (MCPs) followed by a one-dimensional resistive anode encoder (RAE).

Microchannel Plates

The MCP is a lead glass plate perforated by an array of 10^4 microscopic channels on its surface, oriented parallel to one another. Surfaces inside of the channels are treated with semiconductor material to provide high secondary electron emission, while the front and rear surfaces are covered with a metallic alloy to allow voltage to be applied across the length of the channels. Upon impact of a charged particle at the input of a channel, secondary electrons are produced and accelerated by the potential difference across the plate. Further electron multiplication occurs when secondaries collide with channel walls while in transit towards the output. The result is an avalanche of electrons with output gains between 10^4 and

10^6 . A chevron detector consists of two MCPs operating in series with electron gains of 10^7 or more for single events (Wiza, 1992). The MCPs used in our chevron assembly were 25 mm in diameter and had 10 micrometer diameter channels. The potential across each plate was maintained at approximately -900 V, for a total of approximately -1800 V across the entire configuration.

The output electrons generated by the MCPs were accelerated towards and collected by the RAE. The charge gathered by the RAE was used to determine the position of events along a single dimension.

Resistive Anode Encoder

The one-dimensional RAE is a resistive sheet. Electrodes on either side of the sheet collect fractions of the total charge deposited. The larger in magnitude the fraction of charge collected at an electrode, the closer the event location was to that electrode. The fraction of charge accumulated at each electrode results in a voltage pulse, the height of which is proportional to the charge collected at that electrode. The relative position of an event is determined by the ratio between the voltage pulse at one electrode and the sum of the voltage pulses at both electrodes (Waggonner, 1990),

$$x = \frac{V_l}{(V_u + V_l)}, \quad (3.1)$$

where x is the relative position along the RAE axis and V_u and V_l are the voltage pulse heights at the upper and lower electrodes, respectively.

The voltage pulses from the electrodes of the RAE, following charge collection, were next analyzed for position information leading to an angular distribution using standard NIM and CAMAC electronics.

Data Acquisition

An electronic block diagram for data acquisition is shown in Figure 9. Signals from the upper and lower electrodes are equivalently amplified by preamplifiers followed by spectroscopy amplifiers. The voltage pulses from both electrodes are summed by the dual sum/invert, then along with the single pulse from the lower electrode, are guided into the energy and position inputs of the position sensitive analyzer (PSA), respectively. Within the PSA, the division in equation 3.1 takes place producing a voltage pulse, (position output) the height of which is proportional to the event location on the RAE. The energy output of the PSA was measured with a ratemeter. These analog signals of the position output are directed into the ADC and transformed to an equivalent digital form. The ADC

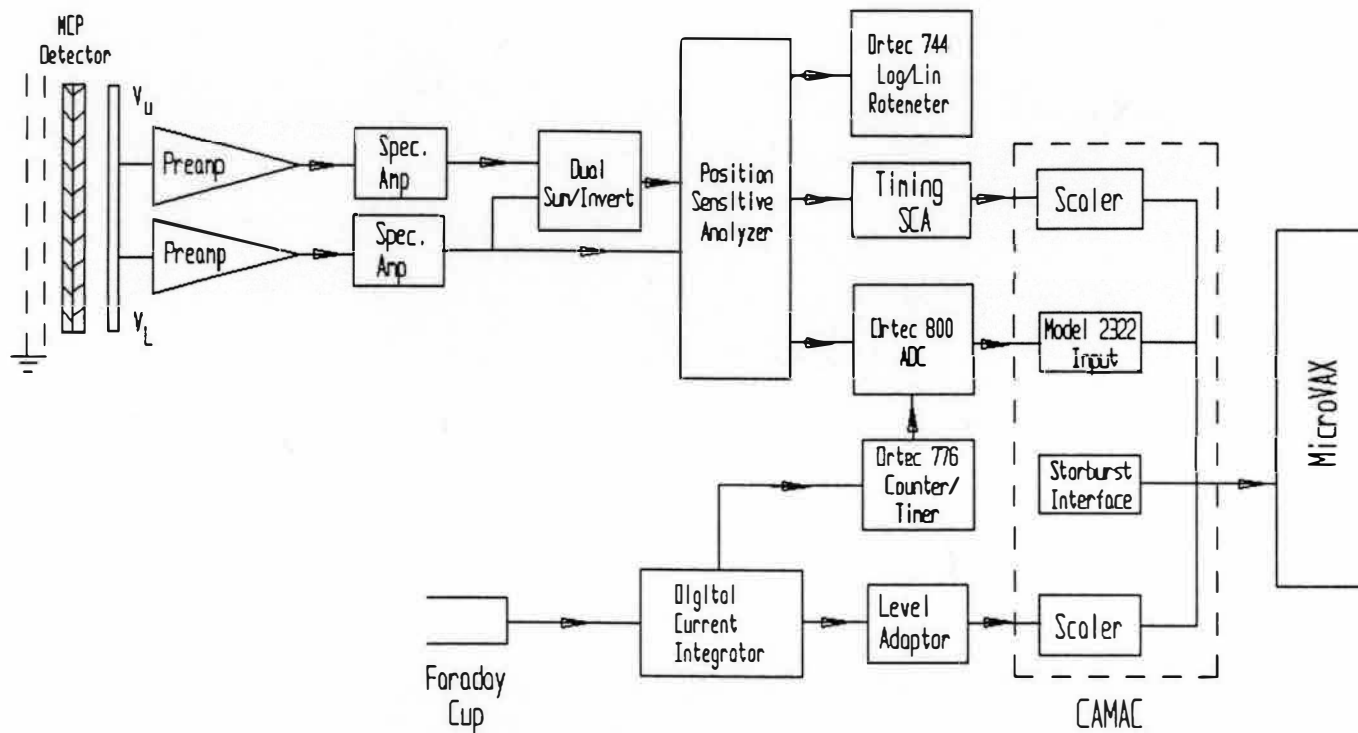


Figure 9. Electronics Block Diagram for Angular Distribution Measurements.

is gated by the counter timer, preset for some maximum number of counts of integrated beam current accumulated by the faraday cup. Digital position signals from the ADC go to the input module of the CAMAC crate. This information is accessed through the STARBURST interface to the microVAX. XPHA, a program on the microVAX, acts as a multichannel pulse height analyzer (PHA). The histogram of the resulting PHA is proportional to $d\sigma/d\theta$. Calibration of the detector involved positioning the direct beam at measured locations from the bow-tie center; recording events at each position allowed the determination of the distance per channel. Together with the measured detector to collision cell distance, the distance per channel permits conversion from a position distribution to an angular one.

A separate electronics configuration was used for calibration of the 180-degree analyzing magnet and retarding grid system. This electronics block diagram is illustrated in Figure 10.

Again, voltage pulses from both electrodes of the RAE were amplified, summed and directed into the PSA. The energy output from the PSA was fed into a single channel analyzer which discriminated the analog signals and converted them to digital ones. A scalar then counted the number of signals resulting from detected ions. For the retarding grid calibration, the scaler continued to count

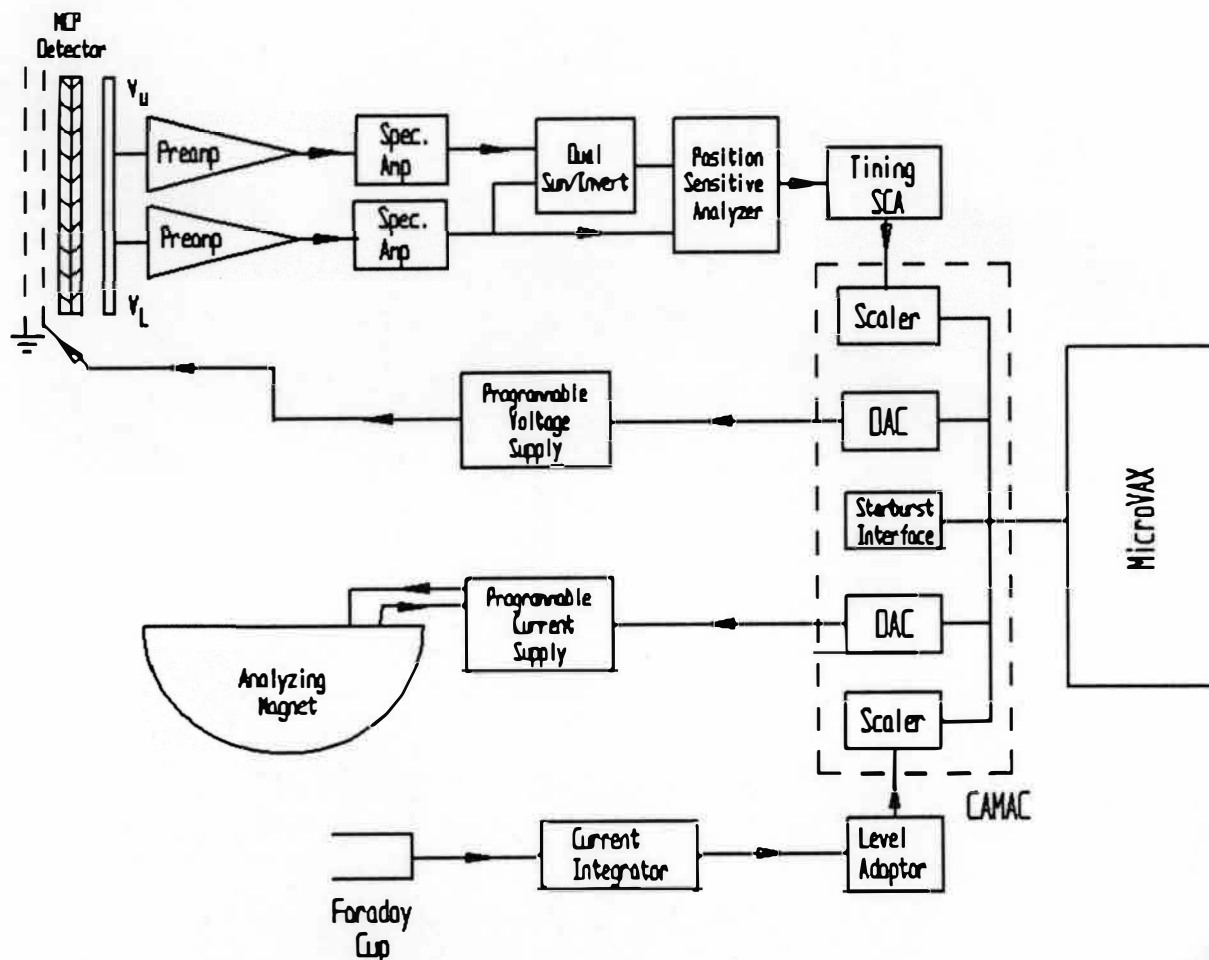


Figure 10. Electronics Block Diagram for Recoil-Ion Charge State Analysis and Retarding Grid Voltage Scans of Reaction Products.

events as the voltage of the grid was varied, while for the analyzing magnet calibration, counts were recorded as the current to the magnet was varied. Another scaler simultaneously counted the number of signals received as a result of integrated beam current collected by the faraday cup. This allowed the signals from the detector to be normalized to the beam current to correct for 'pump beam' fluctuations. For either calibration a microVAX program called KSCAN was employed. Digital signals were given by KSCAN to two DACs which were used to control the voltage and current supplies to the grid and magnet, respectively. These signals were the result of input into the KSCAN program by the user to set the range of the scan, increment it, and choose the number of loops over which the scan was to be performed. While the scan was being executed, KSCAN recorded data from the scalars, producing a histogram of the resulting spectra. The spectra of the retarding grid, as mentioned in a previous section, enabled one to choose the potential necessary to isolate components of the reaction products. The analyzing magnet spectra displayed the intensity of detected events at various currents, thus allowing selection of a particular charge state for the projectile ion beam.

CHAPTER IV

DATA ANALYSIS

Measurements have been made of the angular distribution of single-electron capture. From the observed spectra, the cross section, differential in scattering angle, $d\sigma/d\theta$, is directly obtained.

Charge-State Spectroscopy

Figure 11 shows a charge-state spectrum for argon

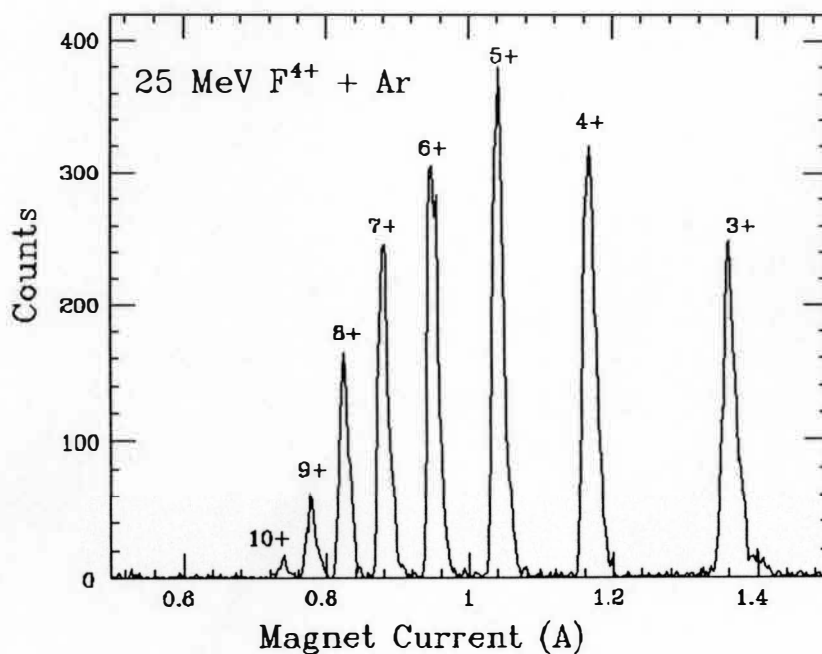


Figure 11. Typical Charge-State Spectrum for Argon Recoil Ions Produced in the Recoil-Ion Source.

recoils. The selection of charge states to be used as recoil projectile ions, produced in the recoil-ion source, required the use of a 180-degree double focussing magnet. Current to the magnet was varied to determine the available charge states. The reason for the smaller sizes of the peaks for charge states 3+ and 4+, is that the detector reached saturation for these charge states during data collection. In order to identify the charge states, a plot was made of the square root of the mass to charge ratio versus the magnet current for each peak. Linearity of this plot was used to test for correct identification (see Figure 12).

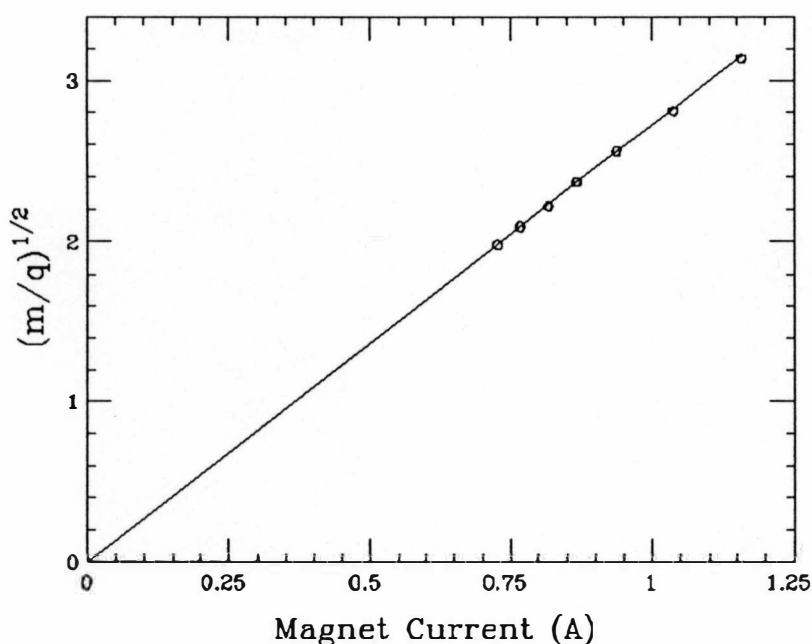


Figure 12. Square Root of Mass-to-Charge Ratio of Argon Recoil Ions Plotted as a Function of the Analyzing Magnet Current.

Energy Analysis

A retarding grid was used to separate components of the products following collision. In order to determine the values to be used for the retarding grid voltages, threshold voltages for the direct beam and single-electron capture had to be determined. The threshold of a beam component represents the voltage for which the component first becomes impeded and thus is equivalent to the average acceleration potential for that component. The relationship between the threshold for the direct beam, V_{db} (average acceleration potential for the direct beam), and the threshold for V_{sec} (average acceleration potential for the single-electron capture component of the beam), can be expressed as

$$V_{db} = \frac{q'}{q} V_{sec} , \quad (4.1)$$

where q and q' are the initial and final charge states of the projectile ion. Figure 13 shows the dependence of the positions of the thresholds on the retarding grid voltage for Ar^{6+} ions incident on He targets. Thus, when collecting data for single-electron capture, voltage for the retarding grid was set at a value existing on the "plateau" between the direct beam and single-electron capture thresholds in order to retard the direct beam (i.e., between 380 and 430

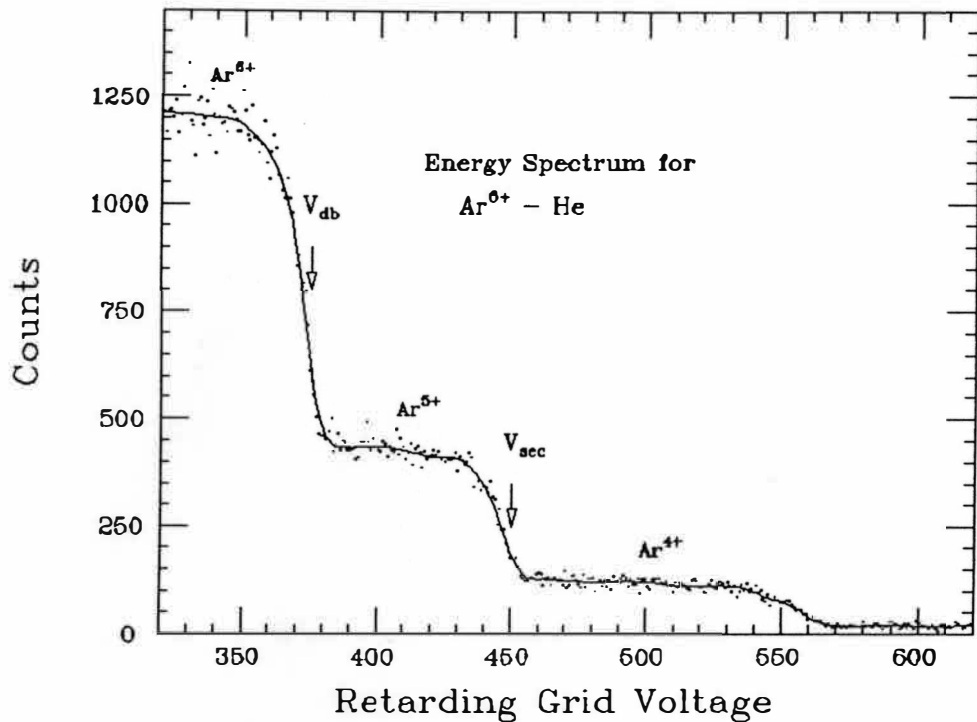


Figure 13. Charge Separation of Product Projectile Ions for the Collision $\text{Ar}^{6+} - \text{He}$.

volts).

Angular Distribution

After collision, the projectile products are collimated by a bow-tie shaped aperture. This aperture approximately converts a radial distribution to a single dimensional one. Therefore, all capture events passing through the collimator contributed to spectra along a transverse axis of the detector. With the center of the bow-tie collimator aligned to the center of the angular distribution, features of the spectra could be correlated with

distances from the bow-tie center. Measurement of the detector-to-collision cell distance then allowed scattering angle calculations associated with specific spectral features, as shown in Figure 14.

The diameter of the detector, 25 mm, was such that the angular limit was less than that of the entire angular distribution. This was observable as scattering from the edge of the detector and was rectified by terminating the spectra at 23 mrad.

In order to calculate the distances between features in a spectrum, a position calibration had to be performed. This was done by positioning the direct beam at measured increments. As mentioned earlier, the entire detector system could be moved both horizontally and vertically via micrometers. Thus, gathering spectra at these positions resulted in a series of peaks of known distances from one

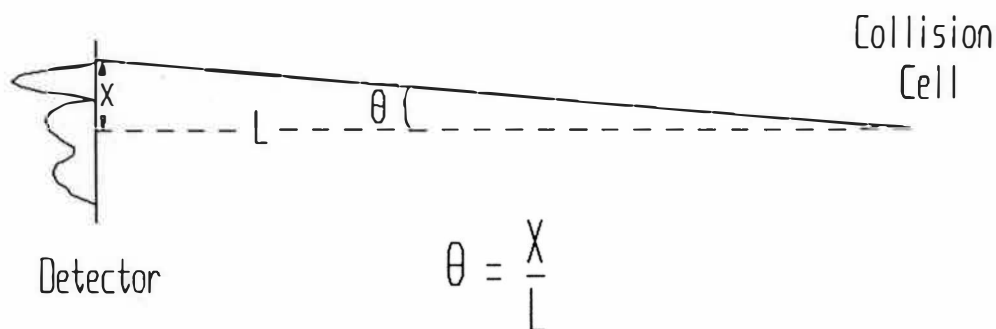


Figure 14. Schematic of the Experiment Showing How Measured Distances Across the Detector Were Converted to an Angular Distribution.

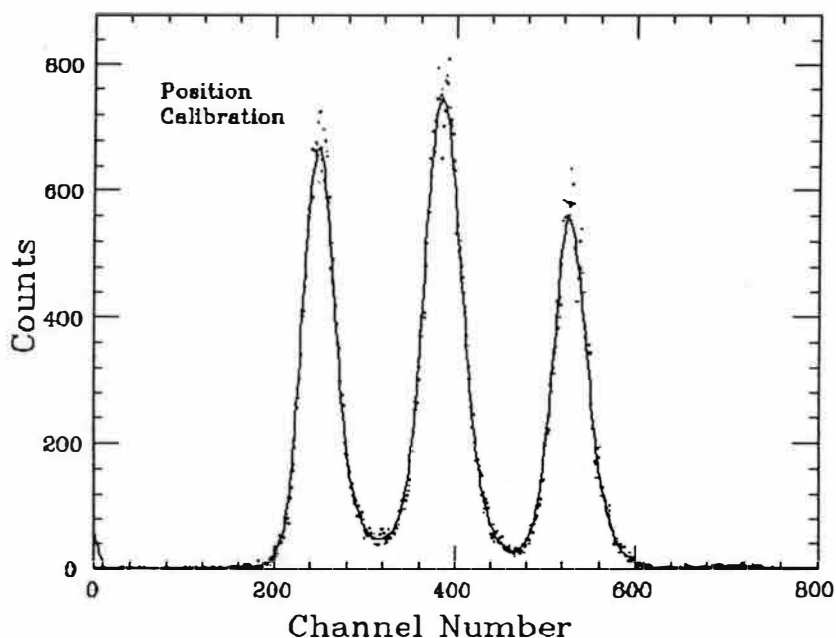


Figure 15. Position Calibration Spectrum Used in the Conversion From Channel Number to Scattering Angle.

another, as shown in Figure 15. The center of each peak corresponds to a unique channel number. Plotting the measured distances versus the channel numbers produced a line whose slope, distance per channel number, allowed for conversion from channel numbers to distances.

Angular Resolution

The angular resolution of the detector system used, i.e., the full-width-at-half maximum (FWHM) of the direct beam was typically around 2 to 3 mrad as displayed in Figure 16.

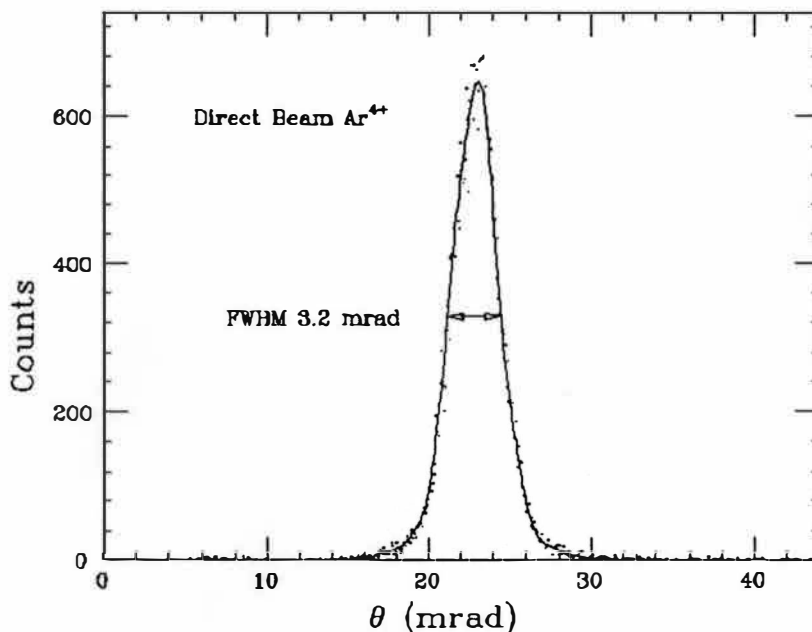


Figure 16. Typical Angular Resolution of an Ar^{4+} Ion Beam.

Background Subtraction

In order to correct for contributions due to background effects in single-electron capture spectra, data were taken both with and without target gas in the collision cell. Spectra obtained from the latter constitutes the background, which, after being normalized to the beam current for the single capture spectra, was subtracted from the "gas in" spectra. Figure 17 displays this process of background subtraction.

For some collision reactions, double-electron capture contributed significantly to the spectra. In these cases, data were obtained for single capture, double capture, and

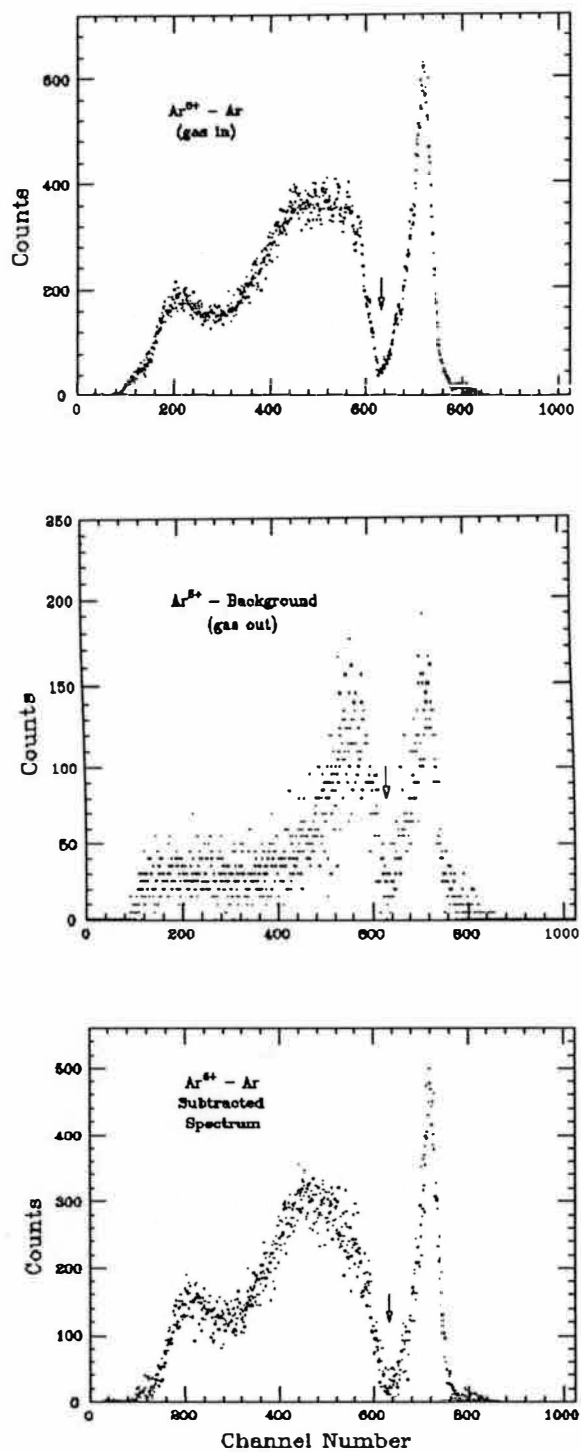


Figure 17. Typical Background Subtraction Process for Angular Distribution Spectra. The Arrows Indicate the Center of the Bow-Tie Collimator.

the background for each. The backgrounds for single and double capture were normalized to the beam current for their respective data runs, and then subtracted from them. Next, the double capture spectrum was normalized to the current collected for single capture and then subtracted from the single capture spectrum. The resulting spectrum thus consisted only of contributions from single capture.

Data Smoothing

As a result of some experimental problems, fluctuations were observed in the experimental spectra obtained. For this reason it was necessary to fit a smoothed curve to the data. This was accomplished using a program called EWA, which fitted the data via Fourier analysis.

Theoretical Calculations

The theoretical model, used to calculate the spectrum for a multi-channel system with capture into a single state, required parameters unique to a particular system. Values for the n and l quantum numbers of the active capture channel and for each open channel of the collision system were needed. The energy defect values were also needed for all reaction channels involved, including the promotion channel. Identification of the states selected for capture was referenced from translational energy-gain

measurements previously reported by other authors. Ionic energy levels and corresponding energy defect values for reaction channels of the collision systems under study were compiled from Bashkin and Stoner (1978), Nielson et al (1985), and Andersson (1986). These values are listed in Tables 1 through 8.

Table 1
Electron Transition Energy Levels Used for
 $\text{Ar}^{4+} (3p^2 \ ^3P) - \text{He}$ Collisions

Projectile Product	Energy Defect $\Delta E(\text{eV})$
$\text{Ar}^{3+} (3p^4 \ ^4P)$	20.47
$\text{Ar}^{3+} (3p^4 \ ^2D)$	17.13
$\text{Ar}^{3+} (3p^4 \ ^2P)$	14.47
$\text{Ar}^{3+} (3p^4 \ ^2S)$	13.19

Source: Bashkin, S., & Stoner, J.O. (1978).

Table 2
Electron Transition Energy Levels Used for
 $\text{Ar}^{5+} (3s^2 \ 3p \ ^2P) - \text{He}$ Collisions

Projectile Product	Energy Defect $\Delta E(\text{eV})$
$\text{Ar}^{4+} (3d \ ^1P)$	19.17
$\text{Ar}^{4+} (4s \ ^3P)$	13.50
$\text{Ar}^{4+} (4s \ ^1P)$	13.07

Source: Bashkin, S., & Stoner, J.O. (1978).

Table 3
Electron Transition Energy Levels Used for
 $\text{Ar}^{6+}(3s^2 \ ^1S) - \text{He}$ Collisions

Projectile Product	Energy Defect $\Delta E(\text{eV})$
$\text{Ar}^{5+} (4s)$	24.29
$\text{Ar}^{5+} (4p)$	17.77
$\text{Ar}^{5+} (4d)$	10.35

Source: Andersson L., (1986).

Table 4
Electron Transition Energy Levels Used for
 $\text{Ar}^{8+}(2p^6 \ ^1S) - \text{He}$ Collisions

Projectile Product	Energy Defect $\Delta E(\text{eV})$
$\text{Ar}^{7+} (4d \ ^2D)$	32.46
$\text{Ar}^{7+} (4f \ ^2F)$	30.07
$\text{Ar}^{7+} (5s \ ^2S)$	18.24

Source: Bashkin, S., & Stoner, J.O. (1978).

Table 5
Electron Transition Energy Levels Used for
 $\text{Ar}^{4+} (3p^2 \ ^3P) - \text{Ar}$ Collisions

Projectile Product	Energy Defect $\Delta E(\text{eV})$
$\text{Ar}^{3+} (4s \ ^2P)$	12.14
$\text{Ar}^{3+} (4s \ ^2D)$	10.80
$\text{Ar}^{3+} (4p \ ^4D)$	8.40
$\text{Ar}^{3+} (4p \ ^4P)$	8.12

Source: Bashkin, S., & Stoner, J.O. (1978).

Table 6
Electron Transition Energy Levels Used for
 $\text{Ar}^{5+} (3s^2 \ 3p \ ^2P) - \text{Ar}$ Collisions

Projectile Product	Energy Defect $\Delta E(\text{eV})$
$\text{Ar}^{4+} (4p \ ^1P)$	17.65
$\text{Ar}^{4+} (4p \ ^1D)$	15.64
$\text{Ar}^{4+} (4p \ ^1S)$	14.48
$\text{Ar}^{4+} (4d \ ^3F)$	9.98

Source: Bashkin, S., & Stoner, J.O. (1978).

Table 7
Electron Transition Energy Levels Used for
 $\text{Ar}^{6+} (3s^2 \ ^1S)$ - Ar Collisions

Projectile Product	Energy Defect $\Delta E(\text{eV})$
$\text{Ar}^{5+} (4d)$	18.9
$\text{Ar}^{5+} (4f)$	15.1
$\text{Ar}^{5+} (5s)$	11.9

Source: E H Nielsen et al. (1985)

Table 8
Electron Transition Energy Levels Used for
 $\text{Ar}^{8+} (2p^6 \ ^1S)$ - Ar Collisions

Projectile Product	Energy Defect $\Delta E(\text{eV})$
$\text{Ar}^{7+} (5d \ ^2D)$	20.54
$\text{Ar}^{7+} (5f \ ^2F)$	19.28
$\text{Ar}^{7+} (6s \ ^2S)$	13.09
$\text{Ar}^{7+} (6p \ ^2P)$	11.94

Source: Bashkin, S., & Stoner, J.O. (1978).

CHAPTER V

RESULTS AND DISCUSSION

In this chapter the individual collision systems for which angular distribution measurements were made are discussed, as well as the results and conclusions subsequently drawn from the data. First, in accordance with the two state curve-crossing model for single-electron capture, half Coulomb scattering angles were determined (see Table 9). These angles, also known as critical angles, are angles corresponding to capture occurring at an impact parameter equal to the crossing radius of the active capture channel, as discussed previously in Chapter II. Qualitative features of the angular distributions and the locations of the main peak with respect to the positions of the critical angle are discussed. Secondly, by making use of the semiclassical multichannel curve-crossing model for single-electron capture, again discussed in Chapter II, theoretical calculations were performed for the angular distributions of $\text{Ar}^{6+,8+}$ ions on He and Ar. The calculated spectra were folded with the experimental resolution and normalized to the heights of the corresponding experimental spectra.

Table 9
Compilation of Data and Results
Using Two-State Model

Collision System	Critical Angle (mrad)	Channel	ΔE (eV)	Crossing Radii (au)
$\text{Ar}^{4+} - \text{He}$	8.20	$3p^4 \ ^2S$	13.19	6.19
		$3p^4 \ ^4P$	20.47	3.99
$\text{Ar}^{5+} - \text{He}$	6.77	$4s \ ^1P$	13.07	8.32
		$3d \ ^1P$	19.17	5.68
$\text{Ar}^{6+} - \text{He}$	7.53	$4p$	17.8	7.64
		$4s$	24.3	5.60
$\text{Ar}^{4+} - \text{Ar}$	6.82	$4p \ ^4D$	8.40	9.71
		$4s^2 \ ^2P$	12.14	6.72
$\text{Ar}^{5+} - \text{Ar}$	6.49	$4d \ ^3F$	11.9	10.90
		$4p \ ^1D$	18.9	6.96
$\text{Ar}^{6+} - \text{Ar}$	5.11	$5s$	9.98	11.43
		$4d$	15.64	7.20

Two-State Model

$\text{Ar}^{q+} - \text{He}$ ($q=4-6$) Collision Systems

Figure 18 displays the differential cross sections for an electron captured from He by Ar^{q+} , ($q=4-6$). For the

collision Ar^{4+} on He at 804 eV, the spectrum exhibits a peak at 11 mrad, lying just outside the critical angle, $\theta_c = 8.20$ mrad. The capture occurs into the excited state $3p^4\ ^2S$ of the Ar^{3+} ion, which is exoergic by 13.19 eV (Yaltkaya et al., 1993). Since this scattering is towards larger angles, most of this distribution can be considered due to capture on the way into the collision. However, because the entrance channel is promoted just inside the active channel ($3p^4\ ^4P$), some of this distribution may also result from capture on the way out of the collision. This happens because electron capture which takes place on the way out may also result in considerable angular deflection by the promoted entrance channel, depending upon the proximity of the promotion. Deflection does not occur if the entrance channel remains flat for a significant distance inside the active crossing.

For 965 eV Ar^{5+} projectile ions capturing an electron from He, there is evidence for both a primary and secondary peak. The primary peak at 10.5 mrad lies outside the critical angle, $\theta_c = 6.77$ mrad, and the secondary peak lies at 18 mrad. The distribution is the result of capture into the $4s\ ^1P$ state of the Ar^{4+} ion, with the $3d\ ^1P$ state being the promoter, as observed by Yaltkaya et al., (1993). Again, with the main distribution lying outside the critical angle, contributions are considered to be from

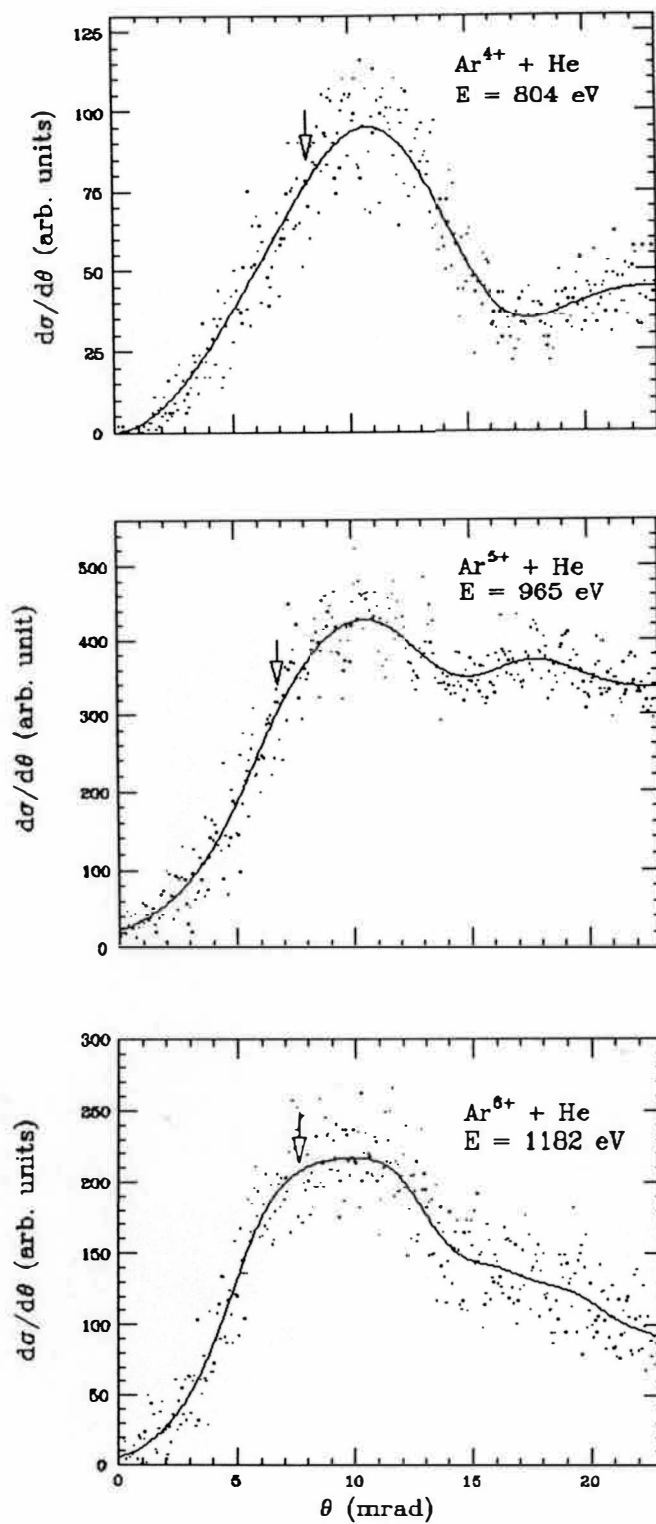


Figure 18. Angular Differential Cross Sections for Ar^{q+} on He for $q = 4-6$. Arrows Indicate Position of θ_c . Data Appear as Points; Smooth Curves are Fits to the Data.

capture occurring on the way into the collision.

At 1182 eV, electrons captured from He by an Ar^{6+} projectile ion result in a broad peaked spectrum. The main peak, at 10 mrad, lies just outside the critical angle, $\theta_c = 7.53$ mrad. Capture occurs into the 4p state of the Ar^{5+} ion, exoergic by 17.8 eV. The promotion channel (4s) lies just inside the active crossing (Andersson, 1986). Consequently, the distribution which seems to consist mainly of contributions due to the upper branch of the deflection function (capture on the way in) may also contain contributions from the lower branch (capture on the way out). The shoulder existing at about 18 mrad is in close agreement with measurements by Waggoner 1990 at 1287 eV.

$\text{Ar}^{q+} - \text{Ar}$ ($q=4-6$) Collision Systems

Figure 19 illustrates the angular differential cross sections for electron capture from Ar by a projectile ion Ar^{q+} , ($q=4-6$). At 616 eV, Ar^{4+} ions capture an electron from an Ar atom, capturing it to the 4p ^4D state. The main peak occurs at 7.5 mrad, just beyond the critical angle at 6.82 mrad. The promotion channel, $4s^2\ ^2\text{P}$, lies near, just inside the capture channel. Thus the distribution is made up of contributions due to both capture on the way into and capture on the way out of the collision.

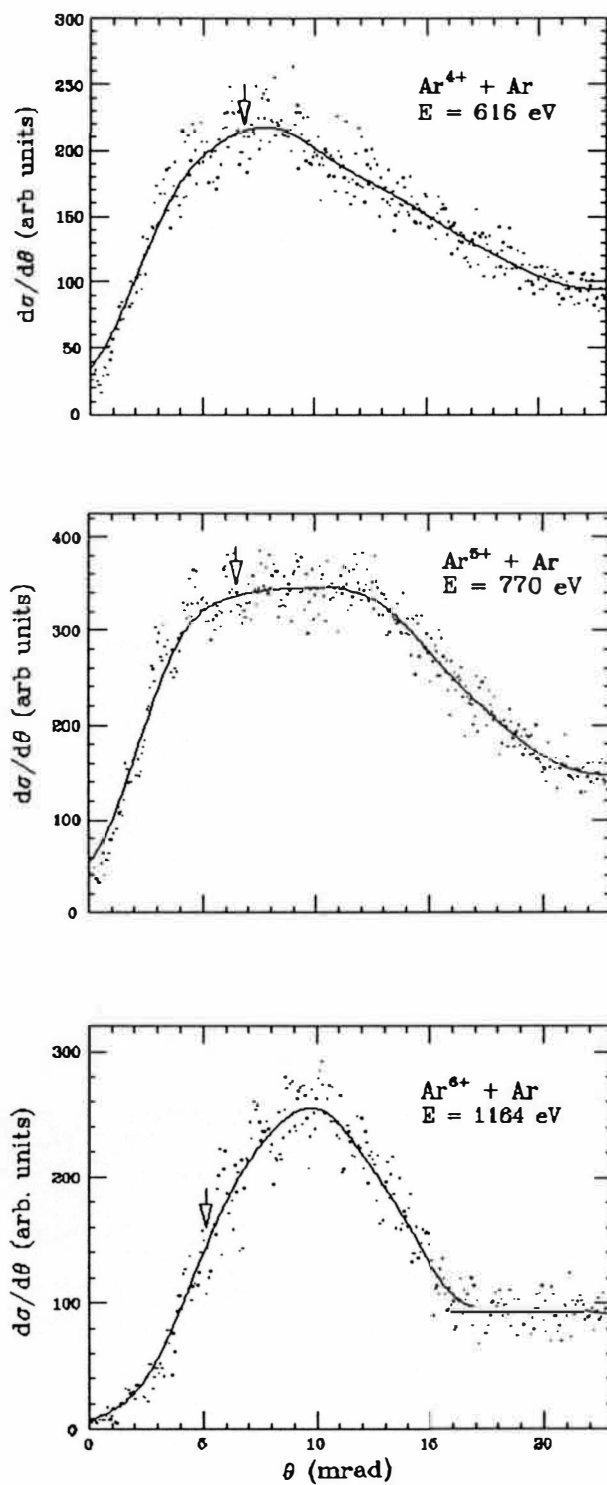


Figure 19. Angular Differential Cross Sections for Ar^{q+} on Ar for $q = 4-6$. Arrows Indicate Position of θ_c . Data Appear as Points; Smooth Curves are Fits to the Data.

For 770 eV Ar^{5+} on Ar collisions, electron capture takes place into the $4d\ ^3F$ state of the Ar^{4+} ion, with the $4p\ ^1D$ state being the collision promoter. The spectrum displays a very broad peak centered at about 9 mrad, lying outside the critical angle of 6.49 mrad. This distribution contains contributions due to capture occurring on the way into collision.

For Ar^{6+} ions capturing an electron from Ar into the 5s state at a collision energy 1164 eV, the spectrum shows a smoothly rising peak at about 10 mrad. The peak lies at a position outside the critical angle of 5.11 mrad and consists of contributions from the upper branch of the deflection function. Contributions from the lower branch are considered to be small, since they should lie at small forward scattering angles.

Semiclassical Multichannel Model

Ar^{q+} - He ($q=6,8$) Collision Systems

Figure 20 shows the measured angular differential cross sections for single-electron capture by Ar^{6+} and Ar^{8+} ions from He at collision energies of 2227 and 2992 eV, respectively. The spectrum for Ar^{6+} on He consists of a main peak centered at 6.8 mrad, outside the critical angle of 4.00 mrad. The theoretical spectrum, folded with the experimental resolution, is presented along with the

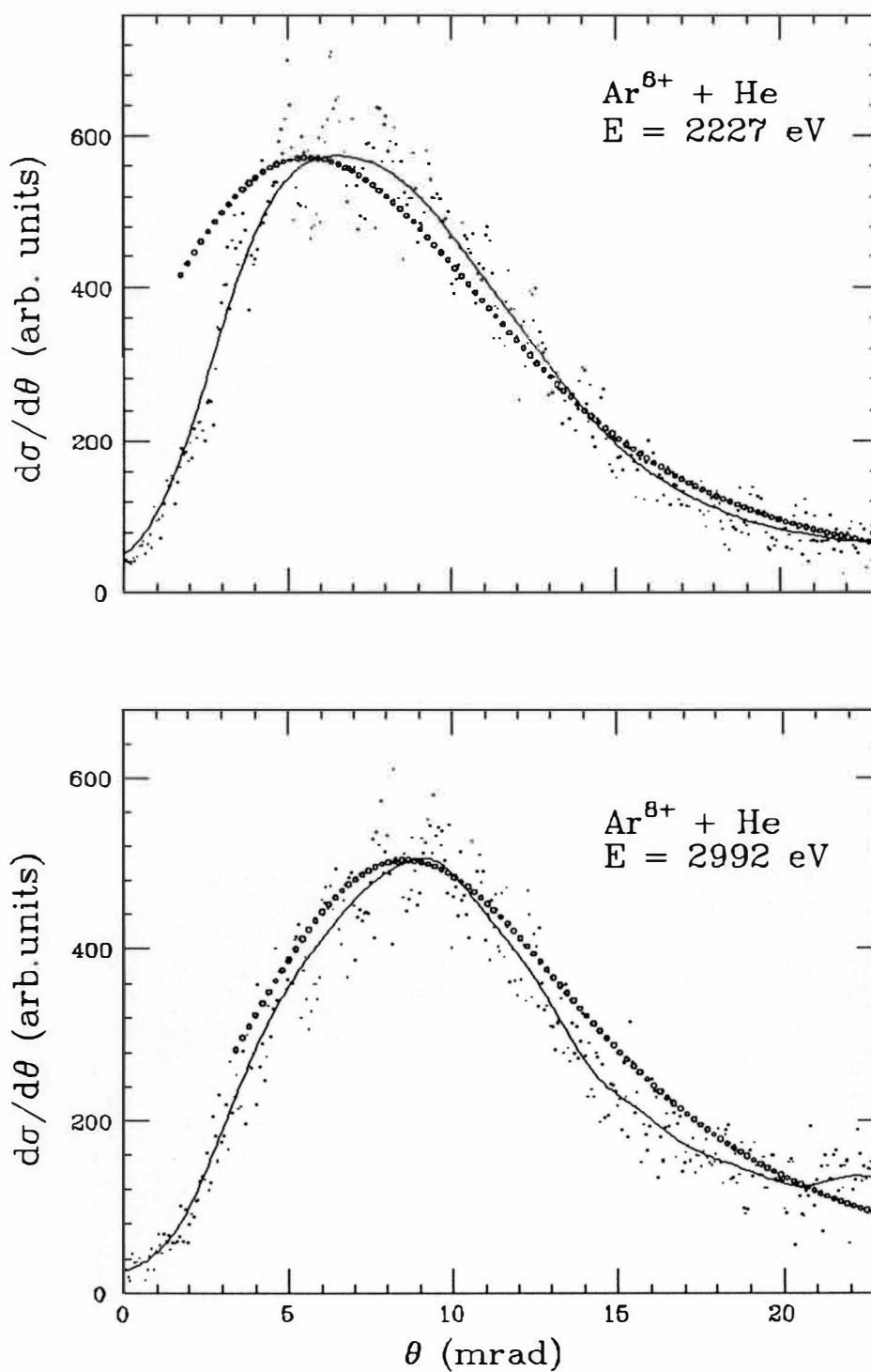


Figure 20. Angular Differential Cross Sections for $\text{Ar}^{6,8+}$ on He. Data Appear as Points, Smooth Curves as Fits and Theoretical Calculations as o's.

experimental findings. Calculations were performed assuming the 4d and 4p states of the Ar^{5+} ion to be open channels, with dominant capture to the 4p state and the 4s state taken to be the promotion channel. The theoretical predictions show close agreement with the measured results, but overestimate the contributions due to smaller angle capture. Waggoner 1990 measured Ar^{6+} on He for single-electron capture at 1287 eV, for which the angular distribution consisted of a main peak lying just inside the critical angle (6.89 mrad) for capture to the 4p state of Ar^{5+} . However, most of their distribution was located outside θ_c , in agreement with our spectrum.

The spectrum for 2992 eV Ar^{8+} ions capturing one electron from He, shows a smoothly rising curve centered at about 9 mrad. Hence, the main peak lies outside the critical angle, $\theta_c = 5.02$ mrad. The calculations were made with 5s and 4f states being the open channels for capture. The primary capture channel was chosen to be 4f and the 4d state was taken to be the promotion channel. The theoretical distribution consists of a peak slightly broader than the measured one, and contributions at larger angles are overestimated.

$\text{Ar}^{q+} - \text{Ar}$ ($q=6,8$) Collision Systems

Spectra for the angular differential cross sections of

Ar^{6+} and Ar^{8+} on Ar for single-electron capture at collision energies of 2226 and 2984 eV, respectively, are shown in figure 21. For single-electron capture from Ar by Ar^{6+} ions, calculations were done assuming the 5s and 4f states to be open channels, with 5s taken as the principal exit channel and 4d as the promoter. The measured spectrum exhibits a primary peak at an angle of 5.5 mrad, with respect to the critical angle of 2.67 mrad. The calculated spectrum nearly fits the position of the main peak, but is a bit broader and overestimates the contributions at larger angles.

For Ar^{8+} ions capturing a single electron from Ar at 2984 eV, the measured angular distribution displays a narrower peak than that predicted by theoretical calculations and lies outside the critical angle of 3.23 mrad. The calculations were done assuming capture into the 6p, 6s, and 5f states of the Ar^{7+} ion. The dominant exit channel was presumed to be 5f, with the 5d state as the promotion channel. On a qualitative basis, the model is a fairly good approximation to the measured spectrum. Cocke et al., (1987) measured angular differential cross sections for single-electron capture for Ar^{8+} on Ar at 1328 eV. They report a main scattered peak outside the critical angle, in agreement with our findings. Although beyond our range of angular measurements, they have also resolved energet-

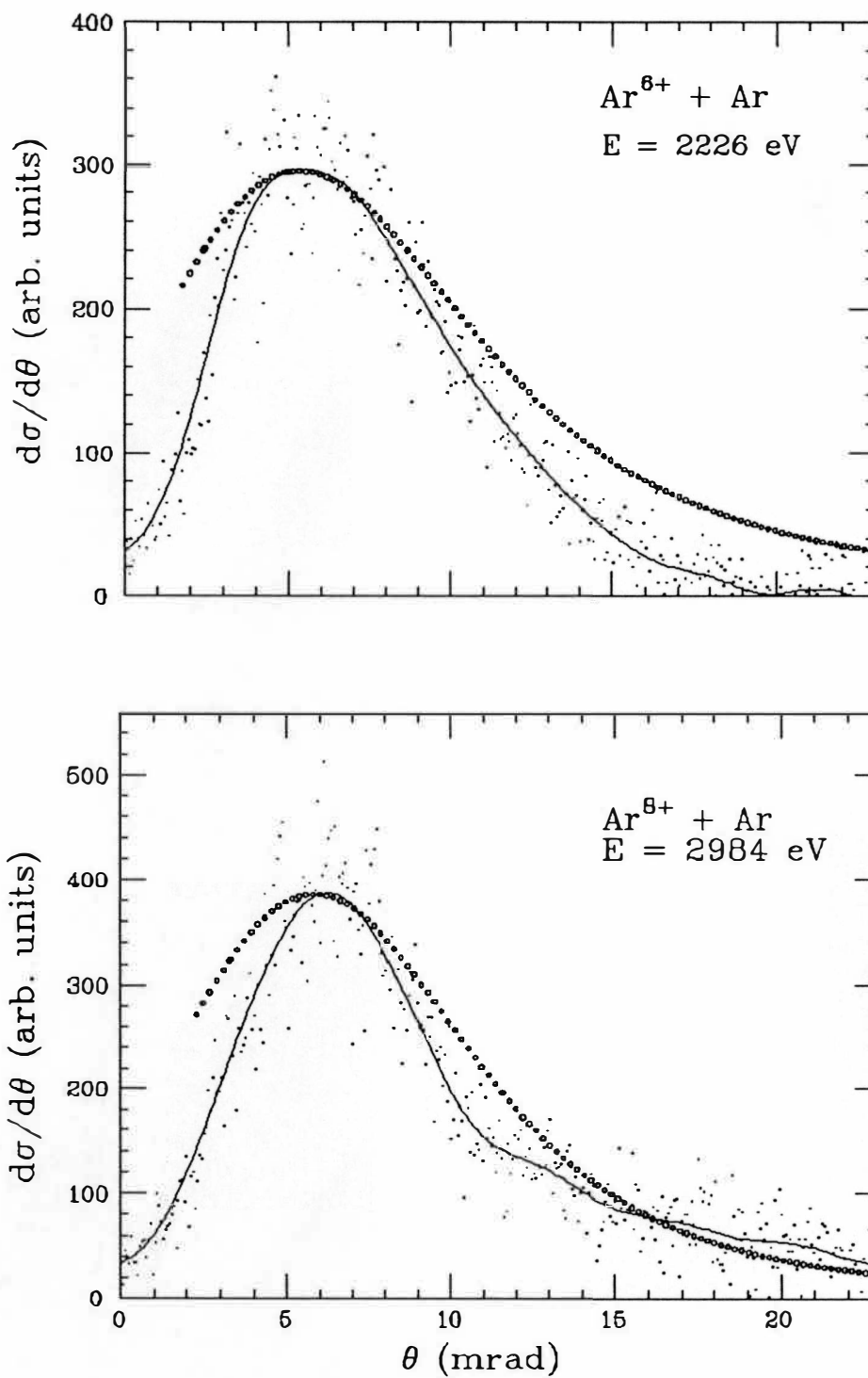


Figure 21. Angular Differential Cross Sections for $\text{Ar}^{6,8+}$ on Ar. Data Appear as Points, Smooth Curves as Fits and Theoretical Calculation as o's.

ically, contributions due to transfer ionization at angles above 20 mrad using a retarding grid analyzer.

CHAPTER VI

CONCLUSION

There were two primary objectives for this thesis. The first intent was to develop a detector assembly capable of measuring angular differential cross sections for ion-atom collisions involving single-electron capture. The second purpose was to investigate the angular distribution for single-electron capture from He and Ar by Ar^{q+} ($q=4-6,8$) projectile ions at energies between 600 and 3000 eV.

The first objective was met. A detector system which included a microchannel-plate detector, a bow-tie shaped aperture, and a retarding grid configuration, was mounted on a chassis which allowed for horizontal and vertical motion under vacuum by way of micrometers. The second purpose was also fulfilled. The angular distribution measurements were fit using Fourier analysis, but detailed structure was not observable. Despite this, the qualitative features of the distributions were still present. Each spectrum consisted of a main peak lying near the critical angle, θ_c , for capture at an impact parameter equal to the crossing radius of the primary capture channel. From calculations of the critical angle, based on the two-state model, for Ar^{q+} ($q=4-6$) on He and Ar, it is observed

that, for most of the spectra collected, the main peak of the distribution lies at angles greater than θ_c . In general, the critical angle is inversely proportional to the collision energy and becomes smaller with increasing energies. Thus, for large collision energies, the distribution should lie outside θ_c . Nonetheless, as explained previously, for diabatic behavior at the initial intersection of the entrance and exit channels, the proximity of the promotion channel must be considered. If the entrance channel is promoted just inside the capture radius, capture results in scattering outside θ_c . If the promotion occurs far inside the active crossing, scattering is forward peaked and takes place at angles less than θ_c . Therefore, one might conclude that the present single-capture contributions were due mainly to capture on the way in, and that for some cases, for which the promoted channel was close to the capture channel, the contributions resulting from capture on the way out were deflected outside θ_c .

For the collision systems for which the semiclassical model was used to calculate spectra, there was qualitative agreement with the positions of the main peak of the angular distributions. Overall it is seen that the model is useful in predicting the qualitative features of the angular distributions.

For future studies predictions using the semiclassical

method might achieve better agreement if, for a particular system, calculations were performed for each open channel. The resulting differential cross sections of each could then be summed and the total calculated spectrum normalized to the experimental measurements.

BIBLIOGRAPHY

- Andersson, L., (1986). Angular Scattering effects in Charge Transfer Collisions between Multiply Charged Ions and Atoms. Research Institute of Physics, Stockholm Report RIPS 86:2.
- Andersson, L.R., Cederquist, H., Barany, A., Liljeby, L., Biedermann, C., Levin, J.C., Keller, N., Elston, S.B., Gibbons, J.P., Kimura, K., & Sellin, I.A., (1991). Simultaneous Single-Electron Capture and Projectile Core Excitation Enhanced through Configuration Interaction in Very Slow Ar^{6+} - He Collisions. Physical Review A **43**, 4075-4078.
- Bashkin, S., & Stoner, J.O. (1978). Atomic Energy Levels and Grottrian Diagrams. Amsterdam: North-Holland.
- Cocke, C.L., (1989). Angular Differential Cross Sections in Low Energy Charge Exchange Collisions. Journal de Physique **50**, 19-28.
- Cocke, C.L., Kamber, E.Y., Tunnell, L.N., Varghese, S.L., & Waggoner, W., (1987b). Angular Distributions of Reaction Products from Low Energy Capture by Multi-charged Ions. Nuclear Instruments and Methods in Physics Research, **A262**, 89-94
- Cocke, C.L., Tunnell, L.N., Waggoner, W., Giese, J.P., Varghese, S.L., Kamber, E.Y., & Pedersen, J.O.K., (1987a). Angular Distributions of Slow Multiply Charged Ions following Capture. Nuclear Instruments and Methods in Physics Research, **B24/25**, 97-100.
- Cooks, R.G., (1978). Collision Spectroscopy. New York: Plenum Press.
- Dalgarno, A., (1985). Charge Transfer Processes in Astrophysical Plasmas. Nuclear Instruments and Methods in Physics Research, **B9**, 655-657.
- Kamber, E.Y., Cocke, C.L., (1991). Ion-Neutral Reactions: Collision Spectrometry of Muticharged Ions at Low Energies. Springer Series in Chemical Physics, **54**, 91-122.

- Leo, W.R., (1987). Techniques for Nuclear and Particle Physics Experiments, Springer-Verlag, Berlin, Heidelberg.
- Loisell, W.H., Scully, M.O., & McKnight, W.B., (1975). Analysis of a Soft X-Ray Laser with Charge Exchange Excitation. Physical Review A11, 989-1000.
- Nielsen, E.H., Anderson, L.H., Barany, A., Cederquist, H., Heinemeier, J., Hvelplund, P., Kundsén, H., MacAdam, K.B., & Sørensen, J., (1985). Energy-Gain Spectroscopy of State-Selective Electron Capture for Multiply Charged Ar Recoil Ions. Journal of Physics B: At.Mol.Phys., 18, 1789-1808.
- Olson, R.E., & Salop, A., (1976). Electron Transfer between Multicharged Ions and Neutral Species. Physical Review A14, 579.
- Taulbjerg, K., (1986). Reaction Windows for Electron Capture by Highly Charged Ions. Journal of Physics B19, 1367.
- Tunnell, L.N., (1986). Ph.D. Dissertation (Kansas State University).
- Tunnell, L.N., Cocke, C.L., Giese, J.P., Kamber, E.Y., Varghese, S.L., and Waggoner, W., (1987). Experimental Angular Distributions for Electron Capture by Slow Ne^{q+} ($q=3-6$) Ions from He. Physical Review A35, 3299-3308.
- Waggoner, W.T., (1990). Ph.D. Dissertation (Kansas State University).
- Waggoner, W., Cocke, C.L., Tunnell, L.N., Havener, C.C., Meyer, F.W., & Phaneuf, R.A., (1988). Angular Distributions for Electron Capture from He by Multiply Charged C, N, O, F, and Ne Ions. Physical Review A37, 2386-2392.
- Wiza, J.L., (1992). Microchannel Plate Detectors, Galileo Electro-Optics Corporation, Sturbridge, MA.
- Yaltkaya, S., Kamber, E.Y., and Ferguson, S.M., (1993). Differential Cross Sections for State-Selective Electron Capture by Low-Energy Ar^{4+} Ions from He and Ar. Physical Review A48, 382.